Document Title:	**Building a Science of Adult Cranial Fracture**
Author(s):	**Todd W. Fenton, Ph.D., Roger C. Haut, Ph.D., Feng Wei, Ph.D**
Document Number:	**300668**
Date Received:	**April 2021**
Award Number:	**2015-DN-BX-K013**

Final Project Overview
Building a Science of Adult Cranial Fracture
NIJ Award No. 2015-DN-BX-K013

Todd W. Fenton[1], Ph.D., Roger C. Haut[2,3], Ph.D., Feng Wei[2,3], Ph.D.

[1]Department of Anthropology
[2]Department of Mechanical Engineering
[3]Department of Radiology
Michigan State University

Table of Contents

Document prepared by Mari Isa, M.A.

Purpose

Adult deaths involving blunt force cranial trauma are challenging cases. Limited foundational data are available to assist medicolegal death investigators in using fracture patterns to locate the point of impact (POI), to determine if injuries are consistent with a single or multiple blows, or to make scientific assessments about implement and energy involved. Much of the available comparative data comes from case studies, which are often based on unsubstantiated accounts of injury causation. This represents a serious gap in best practice in forensic death investigations. Over the last decade, forensic science research has experienced a push to generate ground truth data with known error rates, in accordance with legal standards for expert testimony. Recently, the Scientific Working Group for Forensic Anthropology (SWGANTH) specifically recognized the need for "collaborative research with a biomechanist doing controlled experimental trauma studies" to address the scientific gap in trauma research.

The purpose of this research was to address this SWGANTH-identified need and provide forensic death investigation experts, including pathologists and anthropologists, with the necessary data to accurately interpret blunt cranial trauma. This project used impact experiments on adult human cadaver heads to generate baseline documentation of the effects of various forensically relevant variables on cranial fracture initiation, propagation, and patterning. Specimen-specific computational models were also utilized to explore a mechanistic basis for the locations of cranial fracture initiation.

Project Subjects

The subjects of this study were 39 isolated, fresh human cadaver heads obtained from the University of Maryland Department of Anatomy and the Michigan State University Department of Anatomy. All specimens were de-identified prior to receipt and were therefore IRB exempt.

This resource was prepared by the author(s) using Federal funds provided by the U.S. Department of Justice. Opinions or points of view expressed are those of the author(s) and do not necessarily reflect the official position or policies of the U.S. Department of Justice.

Energy, Implement, and Impact Number Effects on Cranial Fracture

Project Design and Methods

Seventy-two impact experiments were performed on 24 head specimens (male, age of 50 or older at death) in order to investigate the effects of implement shape, input energy, and impact number on cranial fracture development. Five specific aims structured this investigation:

Specific Aim #1: Perform free-motion single impacts at a base or relatively "low" energy

Free-motion impact experiments were conducted on 12 heads using a custom-designed pneumatic system built during the granting period. In this system, compressed gas powered a pneumatic striker, which in turn provided the initial velocity to the impactor. Experiments performed using this system were referred to as "free-motion" because heads were attached to the system in a way that allowed them to move after impact. Each head was secured to a support plate at the C4 vertebra and supported in an upright position with tethers made of 4-lb fishing line. These tethers broke on impact, allowing the head to rotate freely about the neck. The system also allowed linear motion; low-friction bearings allowed the support plate holding the head to slide away from the impactor after impact.

Impacts were delivered to the low mid-parietal, superior to the squamosal suture, using three different shaped aluminum implements: a 1-inch diameter flat surface simulating the shape of a **hammer**, a 3-inch diameter flat implement simulating the shape of a **brick** or flat surface, and a 2.5-inch diameter cylindrical surface simulating the shape of a **baseball bat**. Four heads were impacted with each implement. Impacts were performed at an average of 103.1±17.5 J. This energy level was considered the base, or relatively "**low**," energy level for these experiments based on the results of previous studies by this research team.

Prior to impact soft tissue was removed from the parietal and surrounding sutures, with the exception of a small island of skin placed at the impact site, to allow for visualization of fracture initiation and propagation. All impacts were filmed at 10,000 frames per second using a high-speed camera (Photron SA1.1) purchased as part of this grant.

Specific Aim #2: Perform multiple free-motion impacts at the low energy level

Two additional impacts were conducted on each of the 12 specimens from Specific Aim #1. After complete documentation of the fracture pattern, subsequent parietal impacts were conducted on each head 1) anterior to and 2) posterior to the first impact site using the same implement and energy used to deliver the first impact.

Specific Aim #3: Perform free-motion single impacts at a relatively "high" energy

Impact experiments were conducted on an additional 12 heads using the same methodology described in Specific Aim #1, but with impact energy increased by a factor of 1.5. This increase was achieved through the addition of mass to the impactor. Impacts were performed at an average of 183.3±15.9 J, which was considered the high energy level.

Specific Aim #4: Perform multiple free-motion impacts at the high energy level

Two additional impacts were conducted on each of the 12 specimens from Specific Aim #3. After complete documentation of the fracture pattern, subsequent parietal impacts were conducted on each head 1) anterior to and 2) posterior to the first impact site using the same implement and energy used to deliver the first impact.

Specific Aim #5: Explore mechanistic basis for fracture patterns using computational models

Prior to impact, high-resolution computed tomography (CT) scans were taken of 18 representative heads. Each scan included a Quantitative Computed Tomography (QCT)

calibration phantom to aid in the assignment of material properties. Specimen geometries were discretized into hexahedral and tetrahedral element meshes for finite element analysis.

Data analysis

Impact Data: Velocity and force-time response data recorded for each impact were used to calculate input energy, energy absorbed by the head, peak impact force, displacement at peak force, and time to peak force. These data were summarized in Appendix 1.

Initiation Data: Photron software was used to generate stills from high-speed video of each specimen just prior, during, and after impact. The location/s and sequence of fracture initiation were assessed for each specimen using these images. Fracture photos and diagrams recorded immediately after each impact were used to supplement video findings regarding the location of fractures relative to the POI. Appendix 2 contained a summary of fracture initiation results.

Fracture Pattern Data: Following experimentation, each cranium was cleaned and reconstructed. A modified craniotomy cut was made to enable ectocranial and endocranial assessments of fracture. Fracture diagrams and reconstructed heads were assessed for fracture type, location relative to the POI, and size. Appendix 3 contained diagrams of fracture results.

Computational Data: QCT calibration of the specimens was performed to relate grey values in the CT scan to modulus values in the bone. These analyses were used to generate heat maps of cranial thickness distributions to compare local and global differences within and between specimens. These heat maps were then qualitatively compared to fracture patterns presented after one impact. Examples of these comparisons can be found in Appendix 4.

Findings

Fracture Initiation and Patterns in Low-Energy Single Impacts (Specific Aim #1)

A key finding from the low-energy single impact experiments (n=12) was the observation of linear fractures initiating peripheral to the POI. High-speed video captured peripheral

initiation in experiments with all three implements (3/4 brick, 3/4 bat, and 2/4 hammer). These fractures initiated at sutures or in bones adjacent to the impact site and traveled a) back toward the POI, b) away from the POI, or c) both. At least one impact with each implement generated peripheral-linear fractures that stayed peripheral as they propagated. As a result, 4/12 experiments (2/4 brick, 1/4 bat, and 1/4 hammer) produced peripheral clusters of linear fractures with no damage at the POI. Correct identification of the POI would be unlikely in these cases.

In contrast to linear fractures, some features occurred only at known impact sites. These features, therefore, should be more reliable indicators of impact site. Circular defects, including concentric and depressed fractures, were observed at the POI in 3/4 hammer, 3/4 bat, and 2/4 brick experiments. Additionally, hammer impacts produced internally beveled "bone plugs" on the endocranial surface of the POI in 3/4 cases. However, bone plugs were largely absent in bat and brick impact experiments at the same energy level.

Fracture Patterns in Multiple Impacts at the Base Energy Level (Specific Aim #2)

A key finding from the low-energy multiple impact experiments was that implement shape influenced the frequency of certain fracture types. Out of the three implements tested, the hammer produced circular defects and endocranial bone plugs more frequently than the bat or brick. Nine of 12 hammer impact sites exhibited depressed or concentric fractures around the POI and 8/12 impact sites exhibited endocranial bone plugs. One or both features were present at the known POI at 11/12 hammer impact sites. In contrast, one or both features were observed in just 6/12 bat and 5/12 brick impacts. At least one impact site was obscured in all brick and bat specimens because 1) fractures were linear and initiated peripheral to the POI; 2) new fractures intersected with those from previous impacts; and/or 3) endocranial defects were not observed.

These results suggest implement shape will influence the likelihood of correct impact site identification in cases involving multiple impacts. Impact location will be easier to identify in focused impacts because these implements more often produce circular defects and endocranial bone plugs. In contrast, impact location will be more difficult to identify in impacts with larger implements because these are more likely to extend and complicate pre-existing fractures, and less likely to produce circular defects and bone plugs.

Fracture Initiation and Patterns in Single Impacts at the High Energy Level (Specific Aim #3)

A key finding from the high-energy impact experiments was that peripheral initiation was observed in 6/12 impacts. High-speed video captured peripheral initiation impacts with all three implements (2/4 brick, 2/4 bat, and 2/4 hammer). This result indicated that peripheral fracture initiation could occur in a variety of impact scenarios including low- and high-energy impacts with various implements. In contrast to impacts at the lower energy level, however, peripheral-linear fractures typically propagated back to the POI in high-energy experiments. Only one experiment (a brick impact) generated a cluster of linear fractures remote from the impact site, indicating this fracture pattern was possible, though unlikely, in high-energy impacts.

Fracture Patterns in Multiple Impacts at the High Energy Level (Specific Aim #4)

A key finding from the high-energy multiple impact experiments was that impact energy and implement shape both influenced the frequency of fracture types. All three implements produced circular defects and bone plugs more frequently in high-energy than low-energy impacts. One or both features were observed in 12/12 hammer, 9/12 bat, and 9/12 brick impact experiments. However, the hammer produced circular defects and bone plugs more frequently than the bat or brick. Circular defects were observed in 12/12 hammer, 9/12 bat, and 9/12 brick impact sites, while bone plugs were observed in 10/12 hammer, 6/12 bat, and 7/12 brick impact

sites. Although high-energy impacts more frequently produced circular defects and bone plugs at known impact sites, the high level of fragmentation involved in these cases presented challenges for identifying POI. Multiple impacts with the larger implements (bat and brick) tended to produce fractures that extended, fragmented, and complicated pre-existing fractures, obscuring features helpful for identifying impact sites. In contrast, the hammer implement produced more discrete, potentially identifiable defects. This was largely because the hammer a) tended to "punch through" the cranium, producing localized depressed fracture and b) produced fewer radiating fractures that could complicate existing fracture patterns.

Computational Modeling (Specific Aim #5)

A key finding of the comparisons between thickness distributions and fracture patterns was that skulls of increased or reduced thickness were found to deviate from the hypothesized fracture pattern for their respective impacting implement. For example, a skull of reduced thickness may exhibit a diffuse fracture pattern whether it was impacted at high or low energy, with a focal or diffuse impacting implement, while a skull of increased thickness may exhibit a remote fracture in an area or reduced thickness independent of impacting conditions (see Appendix 5, Figure 1). This suggests that local and global skull thickness may be a confounding variable when attempting to identify the nature of an impacting implement from the resulting fracture pattern alone.

A key outcome of this project was the generation of whole-skull primarily hexahedral finite element meshes. Preliminary quasistatic comparison studies performed under similar loading conditions demonstrate improved stability of hexahedral elements compared to the previously utilized tetrahedral meshes. An example of a primarily hexahedral mesh with a comparison to a tetrahedral result is shown in Appendix 5, Figure 2. Dynamic simulations using

the improved hexahedral models can be used in quantitative investigations of tensile strength distributions in simulated impacts involving focal vs. diffuse loads, different locations of load application, and taking into account variations between skull specimens.

Constraint Condition Effects on Cranial Fracture

Project Design and Methods

Single impacts were performed on an additional 15 heads in order to assess whether constraint condition influenced the initiation of cranial fractures at or peripheral to the point of impact. Two methodologies were used to perform impacts. Five entrapped impacts were performed using a gravity drop impact system designed and built as part of a previous NIJ grant (Award 2007-DN-BX-K196). In this system, specimens were positioned for impact within a rigid (plaster of Paris) medium. The five impacts performed during the current granting period were added to seven entrapped experiments performed as part of an earlier pilot study. In total, twelve entrapped experiments were conducted using the following implements: a 1-inch diameter spherical implement (n=2), a 2-inch diameter hemispherical implement (n=3), a 1-inch square flat implement (n=4), and. a 3-inch diameter flat implement (n=3). Ten free-motion impacts were performed using the above-described pneumatic system. Specimens were impacted once at the center parietal using three of the same implements from the entrapped impacts: the 2-inch hemisphere (n=3), the 1-inch square (n=3), and the 3-inch flat implement (n=4).

Data analysis

Analyses were performed for these 22 impact experiments in the same manner described for the low-parietal impact experiments. The relevant data can be found in Appendices 6-9.

Findings

The key finding of this set of experiments was that fractures initiated peripherally in both free-motion and entrapped impacts. In entrapped impacts, the 1” sphere tended to produce

depressed fractures at the POI while the 3" flat implement produced peripheral-linear fractures. The 1" square and 2" hemisphere seemed to represent transitional implements that produced a mixture of POI and peripheral initiating fractures. In the free-motion impacts, however, impacts with all three implements produced some peripheral and some POI initiating linear fractures. This indicates that cranial fracture initiation likely occurs in a more complex manner than typically described in the literature, with fractures often initiating at several sites simultaneously.

Relationship between Impact and Fracture Location in Mandible Impacts

Project Design and Methods

In addition to cranial impact experiments, mandibular impact experiments were performed on 13 intact heads with the goal of generating baseline data as to the relationship between impact location and fracture location. Mandible impacts were performed only on non-edentulous specimens following the completion of cranial impact experiments. A 1-inch long, 2.5-inch diameter cylindrical implement (mass=6.45 kg) was chosen to simulate a clenched fist impact. Impacts were delivered to five locations as follows: midline (n=3), anterior body at the canine (n=3), mid-body at M1 (n=2), posterior body at M3 (n=2), and ramus (n=3).

Data analysis

Analysis of impact data was performed for mandibular impacts as described for cranial impact experiments. These results can be found in Appendix 10. Post-impact, each mandible was resected and macerated. Fracture numbers and locations were assessed on clean, dry specimens. AOCMF standards were applied in assigning fractures to one of nine regions including the left and right condylar processes, coronoid processes, bodies, and angles, and the symphysis.

Findings

One key finding was that impact location appeared to influence the number of fractures produced. Mandibular body impacts were the only experiments to produce fractures in exactly

one location (5/7 experiments). In contrast, all ramus and midline impacts generated multiple fractures. Another key finding was that mandibular impacts produced at least one fracture approximately at the impact site. In contrast, considerable variation was observed in the location of additional (non-impact site) fractures. More detailed results can be found in Appendix 11.

Implications

This study contributes much-needed foundational data linking fracture patterns with known impact variables including implement, energy, number of impacts, location of impacts, and constraint condition. This unique dataset provides a valuable resource for comparing unknown trauma encountered in forensic cases to known trauma generated through scientific experiments, thereby enabling death investigators to more effectively interpret blunt force cranial and mandibular fracture patterns. To date, the key findings of this project have been disseminated to relevant audiences at various national and international conferences. Appendix 12 contains a complete list of scholarly products stemming from this work, including citations and abstracts from six conference presentations (five accepted and presented, one submitted and under review).

Finally, this work provides a template for future experimental trauma research, an area still in its infancy in the field of forensic science. Future experiments are necessary to explore fracture initiation, propagation, and patterns in other areas of the cranium including the occipital, frontal, and facial bones.

Appendices for Final Project Overview
Building a Science of Adult Cranial Fracture
NIJ Award No. 2015-DN-BX-K013

Todd W. Fenton[1], Ph.D., Roger C. Haut[2,3], Ph.D., Feng Wei[2,3], Ph.D.

[1]Department of Anthropology
[2]Department of Mechanical Engineering,
[3]Department of Radiology
Michigan State University

Table of Contents

Appendix 1: Impact Data for Multiple Impact Experiments

Specimen	Implement	Energy	Impact Number	Trolley Mass (kg)	Pre-Impact Velocity (m/s)	Post-Impact Velocity (m/s)	Input Energy (J)	Energy Absorbed (J)	Overall Peak Force (N)	Displ-acement at Peak Force (mm)	Time to Peak Force (s)
16-3779	Hammer	Low	1	6.05	6.03	4.12	110.0	58.6	5248.0	8.20	0.0014
16-3779	Hammer	Low	2	6.05	6.00	4.62	108.9	44.3	3145.2	5.94	0.0010
16-3779	Hammer	Low	3	6.05	4.33	2.75	56.7	33.8	2368.8	7.18	0.0019
17-0006	Hammer	Low	1	6.35	5.79	3.81	106.2	60.2	5723.1	3.41	0.0006
17-0006	Hammer	Low	2	6.35	6.06	5.16	116.5	32.0	2896.8	3.60	0.0006
17-0006	Hammer	Low	3	6.35	5.28	4.01	88.4	37.4	4048.0	2.64	0.0005
17-3757	Hammer	Low	1	6.35	5.85	4.38	108.6	47.7	10855.6	5.08	0.0009
17-3757	Hammer	Low	2	6.35	6.03	4.38	115.4	54.5	6433.0	4.66	0.0008
17-3757	Hammer	Low	3	6.35	6.64	4.72	139.9	69.4	8055.2	5.14	0.0008
17-3827	Hammer	Low	1	6.35	5.89	4.15	110.1	55.5	5697.3	7.90	0.0014
17-3827	Hammer	Low	2	6.35	5.80	3.97	106.7	56.7	3695.0	5.67	0.0010
17-3827	Hammer	Low	3	6.35	5.82	3.62	107.5	65.9	4833.9	5.17	0.0009
16-3803	Bat	Low	1	6.24	5.98	4.46	111.6	49.5	4877.4	6.37	0.0011
16-3803	Bat	Low	2	6.24	5.97	4.75	111.2	40.8	3435.7	2.95	0.0005
16-3803	Bat	Low	3	6.24	6.03	3.90	113.4	66.0	4414.5	10.69	0.0019
17-2067	Bat	Low	1	6.54	5.77	3.40	108.8	71.0	8581.9	5.91	0.0011
17-2067	Bat	Low	2	6.54	5.61	3.48	102.9	63.4	6021.7	4.28	0.0008
17-2067	Bat	Low	3	6.54	5.72	3.05	107.0	76.6	5090.5	4.77	0.0009
17-3758	Bat	Low	1	6.24	6.03	4.33	113.4	54.9	4824.4	4.14	0.0007
17-3758	Bat	Low	2	6.24	6.10	4.27	116.1	59.2	3336.6	4.20	0.0007
17-3758	Bat	Low	3	6.24	6.06	3.85	114.6	68.5	3256.6	12.08	0.0021
17-4813	Bat	Low	1	6.24	5.95	4.40	110.5	50.0	6134.4	3.49	0.0006
17-4813	Bat	Low	2	6.24	6.17	4.30	118.8	61.0	5100.0	4.85	0.0008

Specimen	Implement	Energy	Impact Number	Trolley Mass (kg)	Pre-Impact Velocity (m/s)	Post-Impact Velocity (m/s)	Input Energy (J)	Energy Absorbed (J)	Overall Peak Force (N)	Displ-acement at Peak Force (mm)	Time to Peak Force (s)
17-4813	Bat	Low	3	6.24	5.99	3.97	111.9	62.9	4550.2	4.70	0.0008
16-3801	Brick	Low	1	6.23	5.60	4.09	97.6	45.6	3695.0	4.42	0.0008
16-3801	Brick	Low	2	6.23	4.22	3.50	55.4	17.3	1786.4	6.26	0.0015
16-3801	Brick	Low	3	6.23	4.39	2.76	60.0	36.3	3693.7	6.89	0.0016
16-3805	Brick	Low	1	6.23	5.25	3.67	85.8	43.9	5067.4	7.11	0.0014
16-3805	Brick	Low	2	6.23	5.40	4.05	90.8	39.7	4965.6	3.73	0.0007
16-3805	Brick	Low	3	6.23	5.26	3.83	86.1	40.5	5705.4	3.10	0.0006
16-3817	Brick	Low	1	6.23	5.52	3.88	94.9	48.0	6693.7	2.68	0.0005
16-3817	Brick	Low	2	6.23	5.49	3.68	93.8	51.7	4075.1	8.22	0.0016
16-3817	Brick	Low	3	6.23	5.62	3.88	98.3	51.5	5773.3	3.29	0.0006
17-2035	Brick	Low	1	6.53	5.96	3.42	115.9	77.7	9591.8	3.44	0.0006
17-2035	Brick	Low	2	6.53	5.78	3.56	109.0	67.7	7027.6	2.73	0.0005
17-2035	Brick	Low	3	6.53	5.82	3.35	110.5	73.9	8614.5	3.96	0.0007
17-2071	Hammer	High	1	9.40	6.16	5.42	178.3	40.5	4178.3	6.53	0.0009
17-2071	Hammer	High	2	9.40	6.14	5.63	177.2	28.3	3615.9	8.60	0.0014
17-2071	Hammer	High	3	9.40	6.05	5.41	172.0	34.7	4194.6	8.91	0.0015
17-2075	Hammer	High	1	9.40	6.14	4.58	177.2	78.6	6671.9	5.58	0.0009
17-2075	Hammer	High	2	9.40	6.28	4.91	185.4	71.9	6904.1	3.87	0.0006
17-2075	Hammer	High	3	9.40	6.24	5.19	183.0	56.6	4937.1	7.26	0.0012
17-2082	Hammer	High	1	9.40	5.79	4.15	157.6	76.8	7367.0	6.74	0.0012
17-2082	Hammer	High	2	9.40	6.03	5.04	170.9	51.6	4379.2	8.07	0.0014
17-2082	Hammer	High	3	9.40	6.24	5.19	183.0	56.4	4216.3	5.65	0.0009
18-2359	Hammer	High	1	9.42	6.51	5.48	199.6	58.2	6270.4	5.86	0.0009
18-2359	Hammer	High	2	9.42	6.56	6.04	202.7	30.9	3152.2	3.59	0.0006
18-2359	Hammer	High	3	9.42	6.01	5.30	170.1	37.8	3114.2	4.51	0.0008

Specimen	Implement	Energy	Impact Number	Trolley Mass (kg)	Pre-Impact Velocity (m/s)	Post-Impact Velocity (m/s)	Input Energy (J)	Energy Absorbed (J)	Overall Peak Force (N)	Displ-acement at Peak Force (mm)	Time to Peak Force (s)
17-2081	Bat	High	1	9.59	6.18	4.29	183.2	95.1	8416.3	6.15	0.0010
17-2081	Bat	High	3	9.59	6.14	2.88	180.8	141.1	3690.9	9.94	0.0017
17-2118	Bat	High	1	9.59	6.28	3.50	189.2	130.3	5267.0	5.00	0.0008
17-2118	Bat	High	2	9.59	6.13	3.59	180.2	118.4	2676.9	8.75	0.0015
17-2118	Bat	High	3	9.59	6.05	3.28	175.6	123.9	3704.5	6.41	0.0011
18-0364	Bat	High	1	9.63	6.33	4.75	192.8	84.2	5230.3	6.05	0.0010
18-0364	Bat	High	2	9.63	6.40	5.69	197.1	41.3	2162.4	3.87	0.0006
18-0364	Bat	High	3	9.63	6.33	5.02	192.8	71.6	3165.8	17.24	0.0028
18-0386	Bat	High	1	9.63	6.23	4.44	186.8	92.0	6920.7	4.78	0.0008
18-0386	Bat	High	2	9.63	6.24	4.62	187.4	84.6	4319.7	10.74	0.0018
18-0386	Bat	High	3	9.63	6.12	4.65	180.2	76.0	4417.4	2.82	0.0005
17-2095	Brick	High	1	9.58	6.29	3.93	189.5	115.4	10806.8	4.68	0.0008
17-2095	Brick	High	2	9.58	6.38	4.76	195.0	86.2	5493.7	9.21	0.0015
17-2095	Brick	High	3	9.58	6.30	3.75	190.1	122.8	7200.0	7.98	0.0013
17-2132	Brick	High	1	9.58	4.93	3.33	116.4	63.5	8387.8	2.15	0.0005
17-2132	Brick	High	2	9.58	5.98	4.74	171.3	63.8	4638.5	3.42	0.0006
17-2132	Brick	High	3	9.58	5.87	3.99	165.0	89.0	8656.5	3.34	0.0006
18-0300	Brick	High	1	9.62	6.30	4.55	190.8	91.1	4645.5	2.11	0.0003
18-0300	Brick	High	2	9.62	6.31	4.92	191.4	75.2	2860.3	14.57	0.0024
18-0300	Brick	High	3	9.62	6.30	4.32	190.8	100.9	3032.7	11.55	0.0019
18-0361	Brick	High	1	9.62	6.44	4.31	199.4	110.1	9607.2	5.68	0.0009
18-0361	Brick	High	2	9.62	6.55	4.94	206.3	88.9	6508.0	2.94	0.0005
18-0361	Brick	High	3	9.62	6.41	5.02	197.6	76.4	4512.4	8.33	0.0013

Appendix 2: Fracture initiation in free-motion impacts to the low mid-parietal.

Interface	Specimen	Initiation
Hammer (n=4)	17-3827	The impact produces a shallow circular depression at the POI.
	17-3757	Peripheral-linear fractures initiate in the inferior temporal bone and propagate superiorly to the squamosal suture.
	16-3779	A linear fracture initiates at the POI and travels to the coronal suture. A diastatic fracture of the sphenotemporal suture forms. Peripheral linear fractures travel from this suture into the temporal bone. The impact also produces a circular depressed fracture at the POI.
	17-0006	A peripheral linear fracture initiates in the temporal and travels back toward the POI. A concentric fracture encircles the POI. Three linear fractures initiate at the POI and propagate away. The longest of these fractures travels toward pterion.
Bat (n=4)	16-3803	A peripheral linear fracture initiates in the anterior parietal and travels in two directions, back to the POI and into the frontal. A semicircular fracture also forms superior to the POI.
	17-4813	A diastatic fracture of the sphenotemporal suture forms. Peripheral-linear fractures initiate at this suture and travel into the temporal, sphenoid, and parietal bones.
	17-3758	Concentric fractures initiate at the squamosal suture and propagate superiorly, encircling the POI. Several peripheral linear fractures initiate and propagate within the temporal bone.
	17-2067	A peripheral linear fracture initiates in the center of the temporal and travels back to the POI. Next, a linear fracture initiates at the POI and travels anteriorly and inferiorly into the sphenoid and frontal. Several peripheral linear fractures initiate at the squamosal suture and propagate into the temporal.
Brick (n=4)	16-3817	Several peripheral linear fractures initiate in the sphenoid.
	16-3805	A peripheral linear fracture initiates at the external auditory meatus and propagates to the squamosal suture. Another peripheral linear fracture initiates at the squamosal suture and travels into the posterior parietal.
	16-3801	Peripheral linear fractures initiate near pterion and propagate both toward and away from the POI. Several POI linear and concentric fractures form, producing extensive fragmentation.

	17-2035	A peripheral linear fracture initiates in the sphenoid, continues as a diastatic fracture of the squamosal suture, and terminates in the parietal near the POI. This impact also produces a concentric fracture around the POI.

Table 1. Initiation results in low-energy impacts.

Interface	Specimen	Initiation
Hammer (n=4)	18-2359	A linear fracture initiates at the POI and travels toward the coronal suture. The implement punches through the cranium.
	17-2082	The impact produces diastatic fracture of the squamosal suture. Short peripheral linear fractures initiate at the squamosal suture and propagate back toward the POI. The impact also produces a depressed fracture at the POI.
	17-2075	The impact produces a diastatic fracture of the squamosal suture. The impact also produces a depressed fracture at the POI.
	17-2071	A peripheral linear fracture initiates at the sphenotemporal suture and propagates through the temporal bone back to POI. A concentric fracture then forms around the POI. Several linear fractures initiate at this concentric fracture and travel in two directions to and away from the POI.
Bat (n=4)	18-0364	A peripheral linear fracture initiates in the anterior temporal and propagates in two directions, back to the POI and to the sphenotemporal suture. Several linear fractures travel away from the POI posteriorly, superiorly, and anteriorly. This impact also produces a concentric fracture around the POI.
	18-0386	A peripheral linear fracture initiates in the temporal, branching and traveling back to the POI. Another linear fracture initiates at the POI and travels anteriorly toward the coronal suture. The impact also produces concentric fractures around the POI.
	17-2081	A linear fracture initiates at the POI and travels into the frontal. The impact also produces concentric fractures around the POI and diastatic fractures of the squamosal and sphenotemporal sutures.
	17-2118	Several linear fractures initiate at the POI, propagating inferiorly into the temporal and superiorly toward the sagittal suture. This impact also produces concentric fractures around the POI.

Brick (n=4)	18-0300	The impact produces a diastatic fracture of the sphenofrontal suture. A peripheral linear fracture forms in the sphenoid as a concentric fracture forms around the POI. Several linear fractures travel from the POI inferiorly into the temporal, anteriorly toward the coronal suture, and superiorly toward the sagittal suture, resulting in extensive fragmentation of the parietal and temporal.
	18-0361	Peripheral linear fractures initiate along the squamosal suture, traveling both toward and away from the POI. A peripheral linear fracture initiates in the inferior temporal and propagates superiorly toward the POI. A peripheral linear fracture initiates anterior to asterion and propagates toward the POI.
	17-2095	Linear fractures initiate at the POI and propagate toward pterion. Additional linear fractures travel from the POI into the temporal, fragmenting the bone. A concentric fracture forms around the POI.
	17-2132	Linear fractures initiate at the POI and propagate toward pterion. Additional linear fractures travel from the POI to the temporal.

Table 2. Initiation results in high-energy impacts.

Appendix 3: Diagrams of fractures in multiple impact experiments.

Fractures associated with the first (mid-parietal) impact are shown in red, fractures associated with the second (anterior) impact in green, and third (posterior) impact in blue.

Low Energy Impact Experiments

Hammer (n = 4)

16-3779

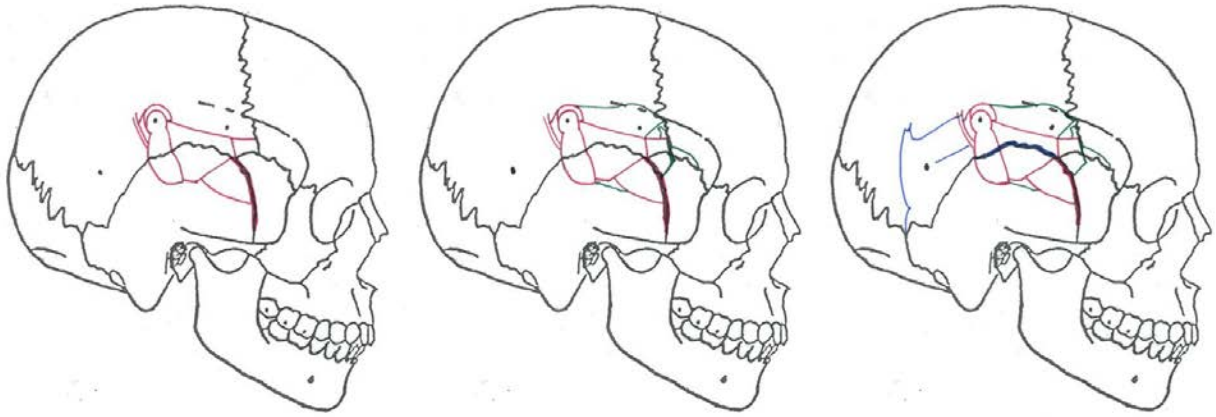

17-0006

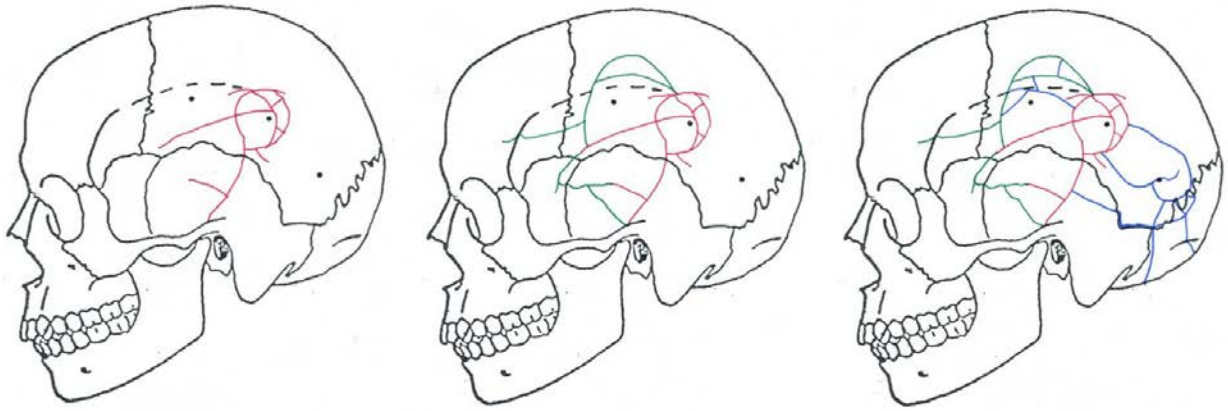

17-3757

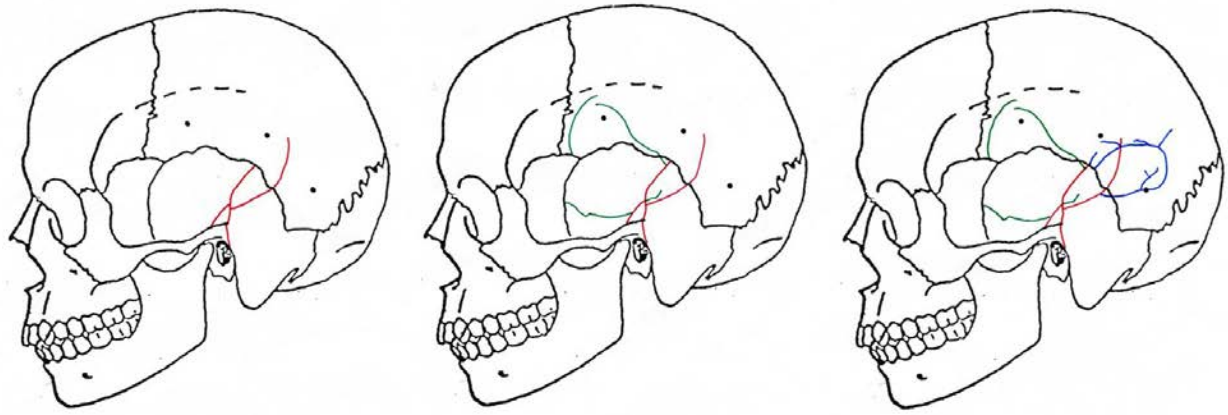

This resource was prepared by the author(s) using Federal funds provided by the U.S. Department of Justice. Opinions or points of view expressed are those of the author(s) and do not necessarily reflect the official position or policies of the U.S. Department of Justice.

17-3827

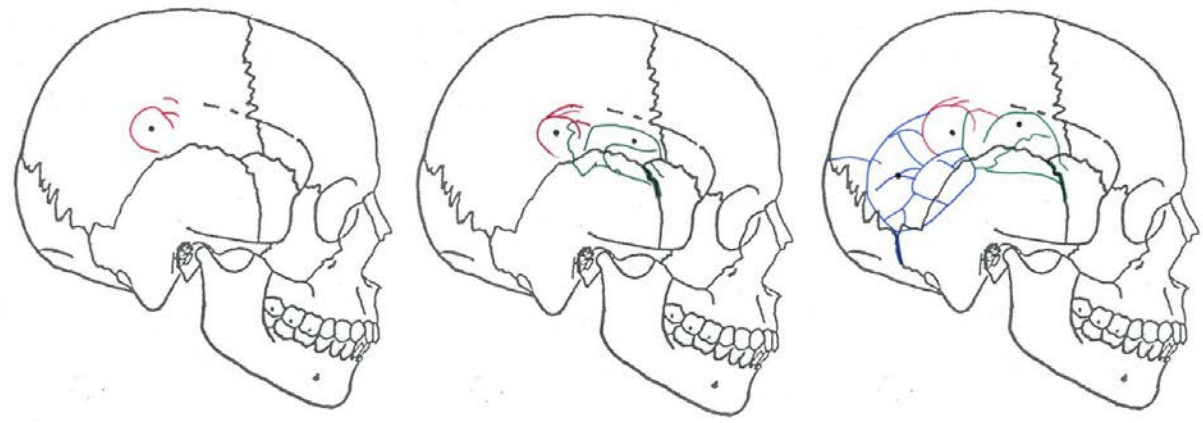

Bat (n = 4)
16-3803

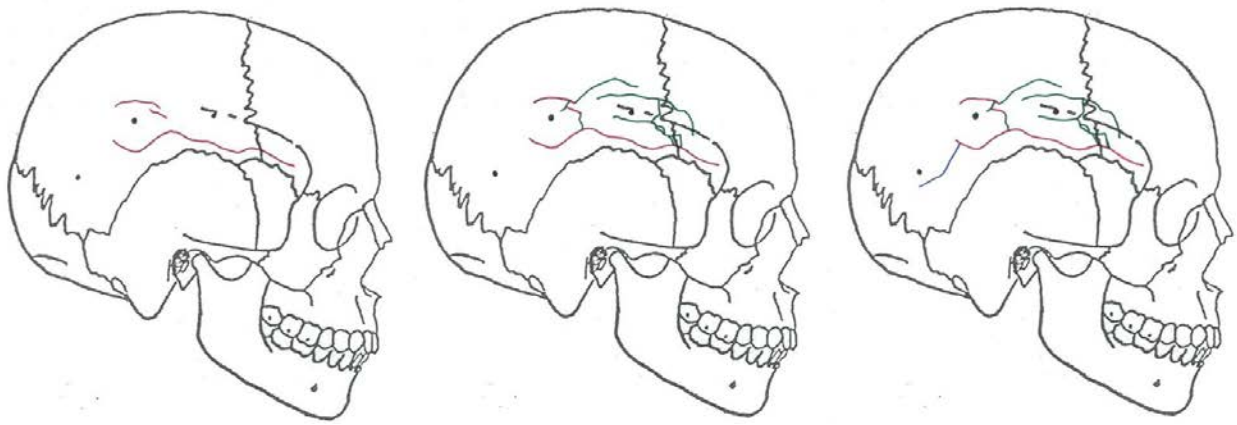

17-2067

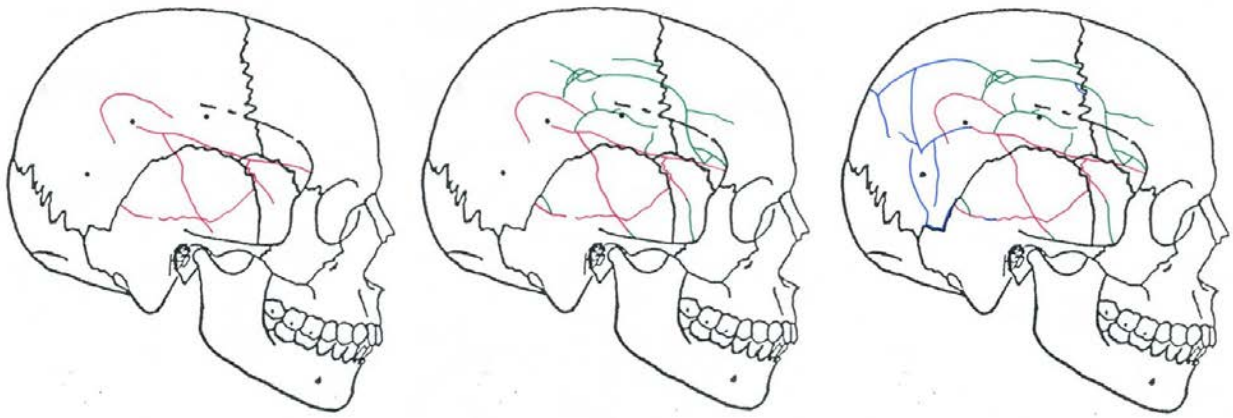

17-3758

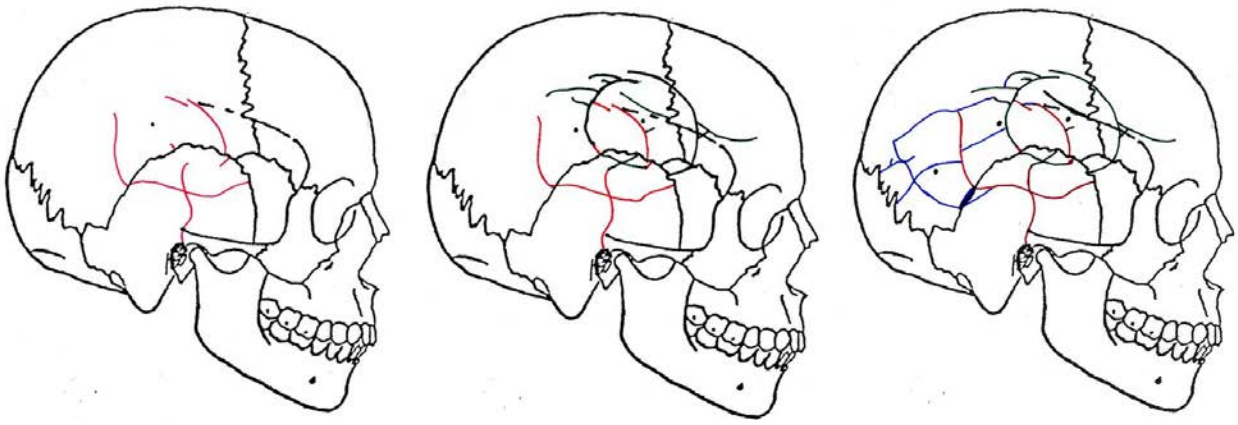

17-4813

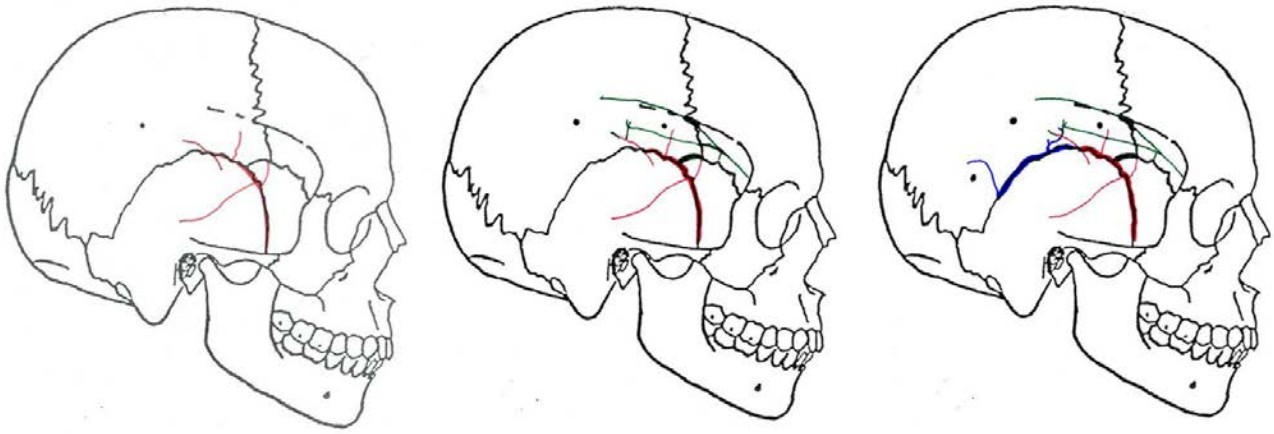

Brick (n = 4)

16-3801

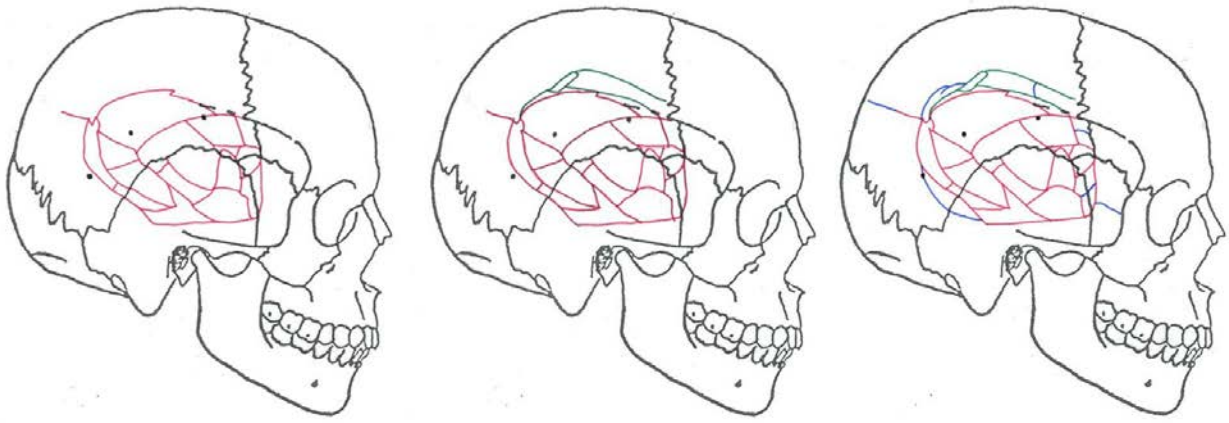

16-3805

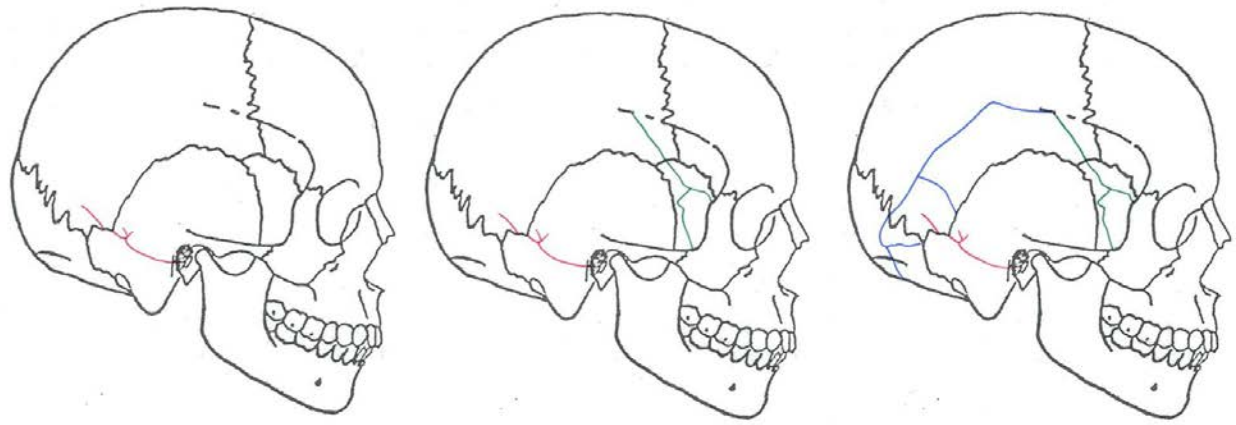

16-3817

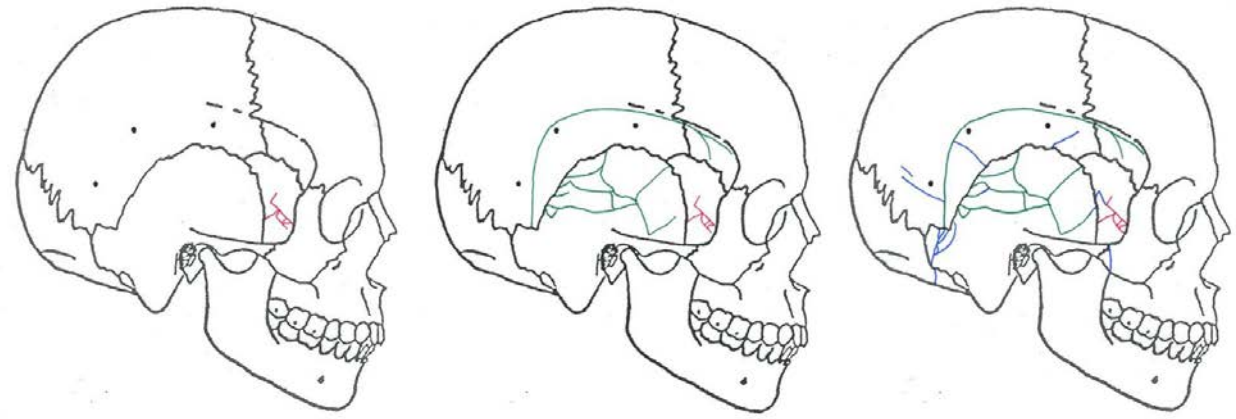

17-2035

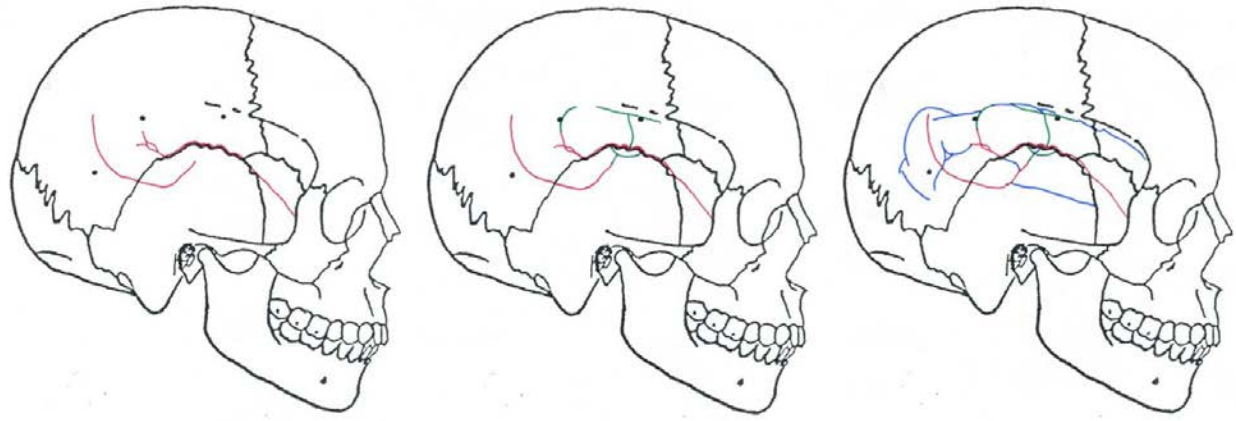

High Energy Impact Experiments

Hammer (n = 4)

17-2071

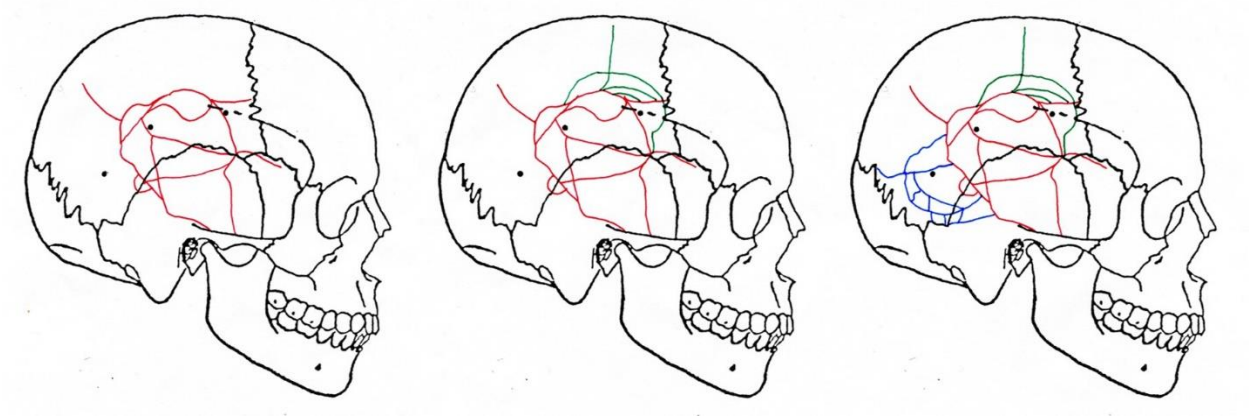

17-2075

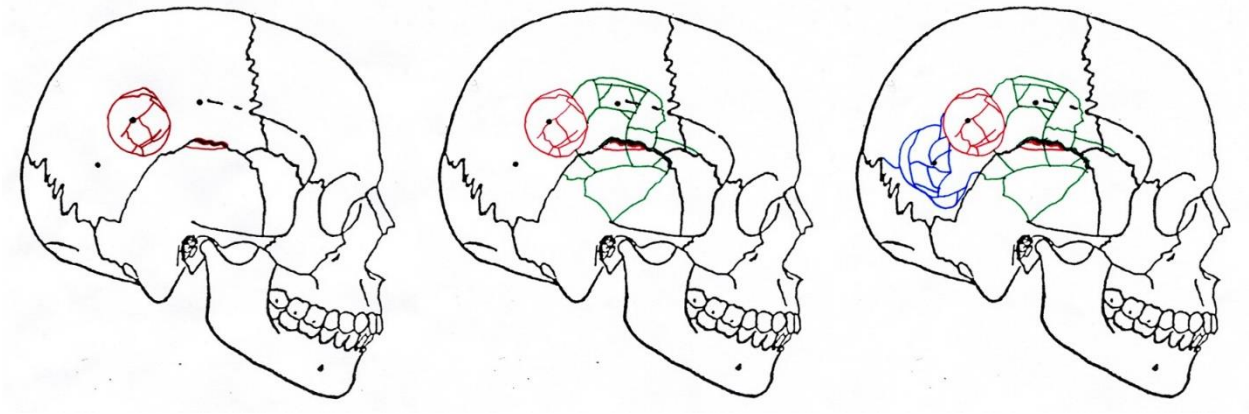

17-2082

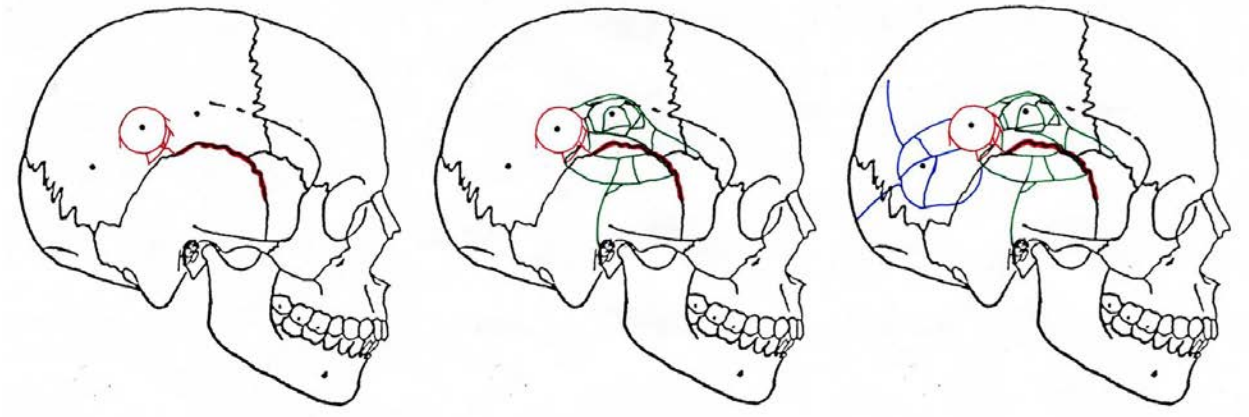

18-2359

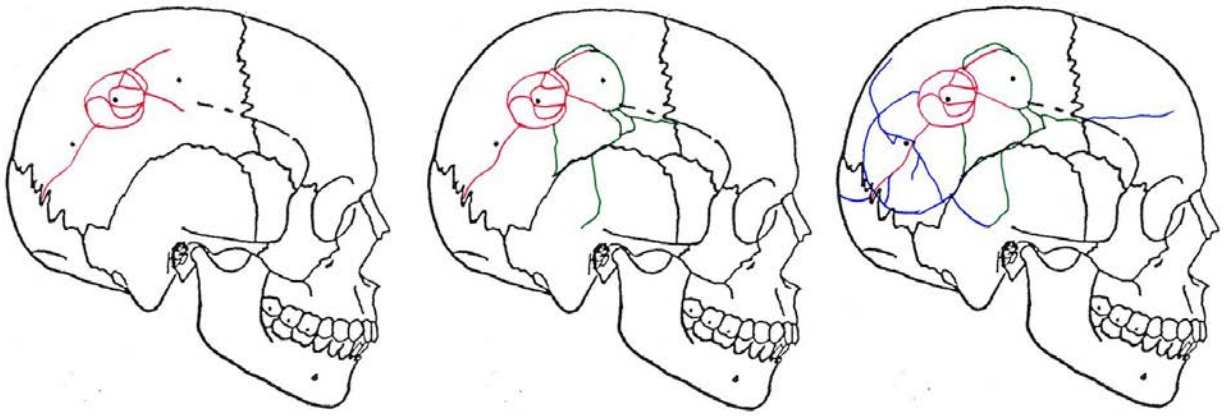

Bat (n = 4)

17-2081

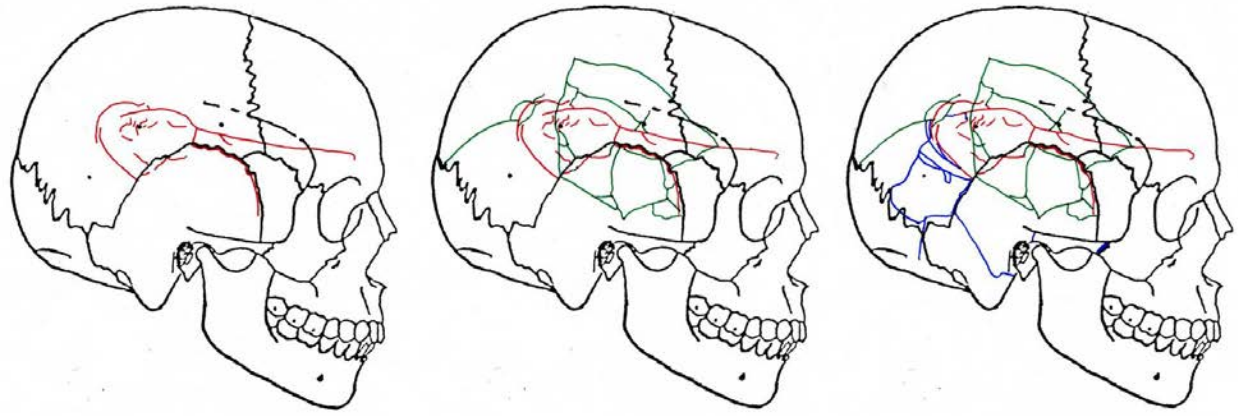

17-2118

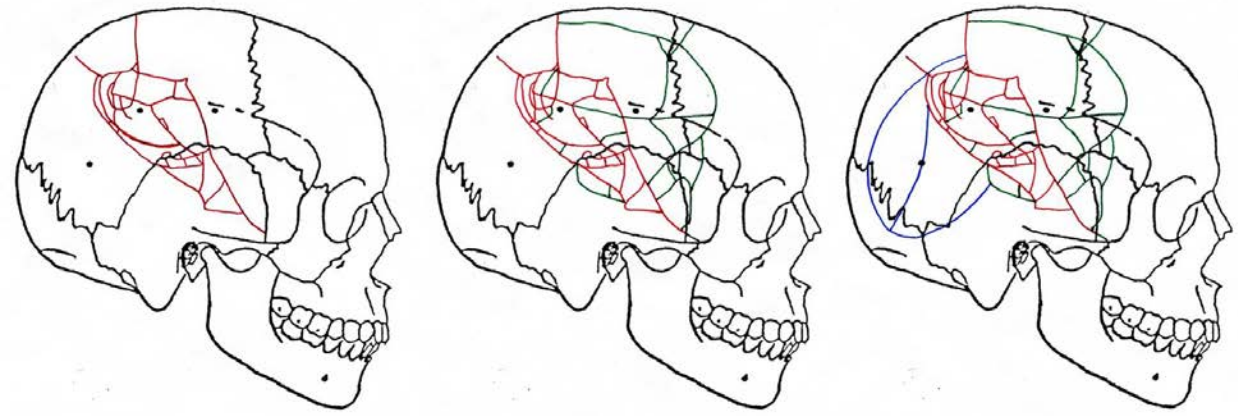

18-0364

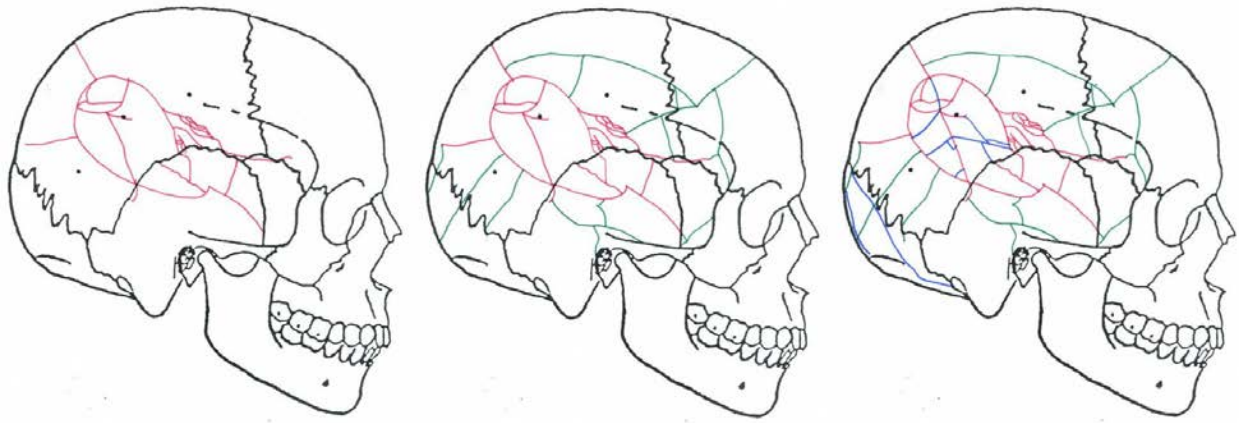

18-0386

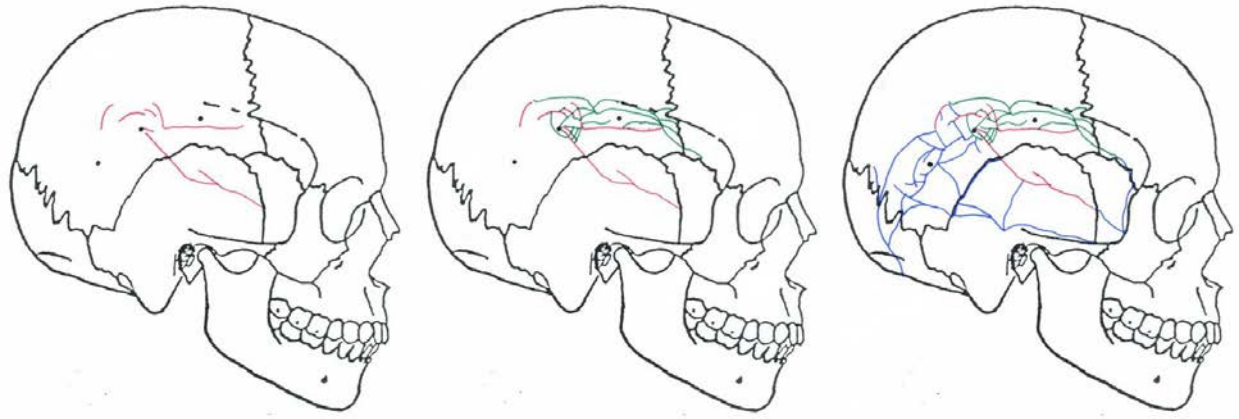

Brick (n = 4)

17-2095

17-2132

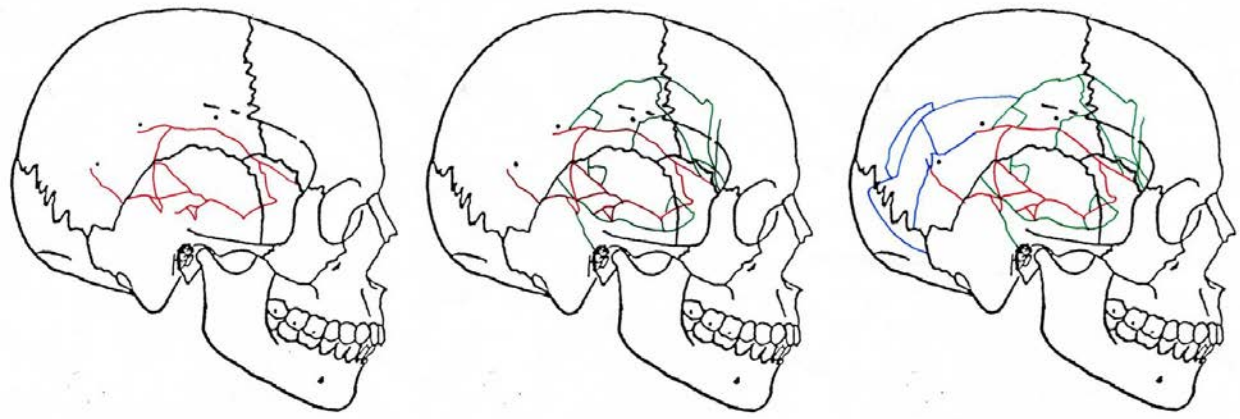

18-0300

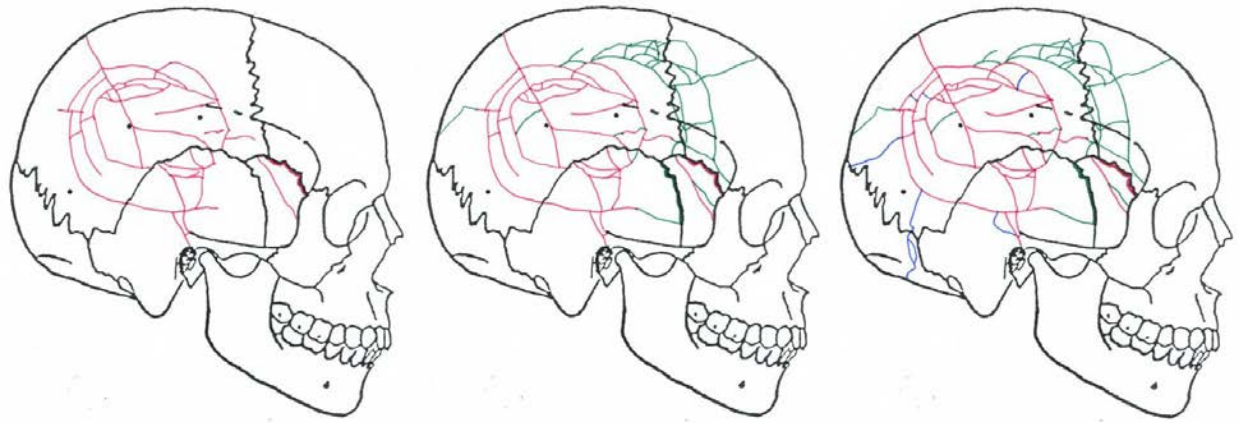

18-0361

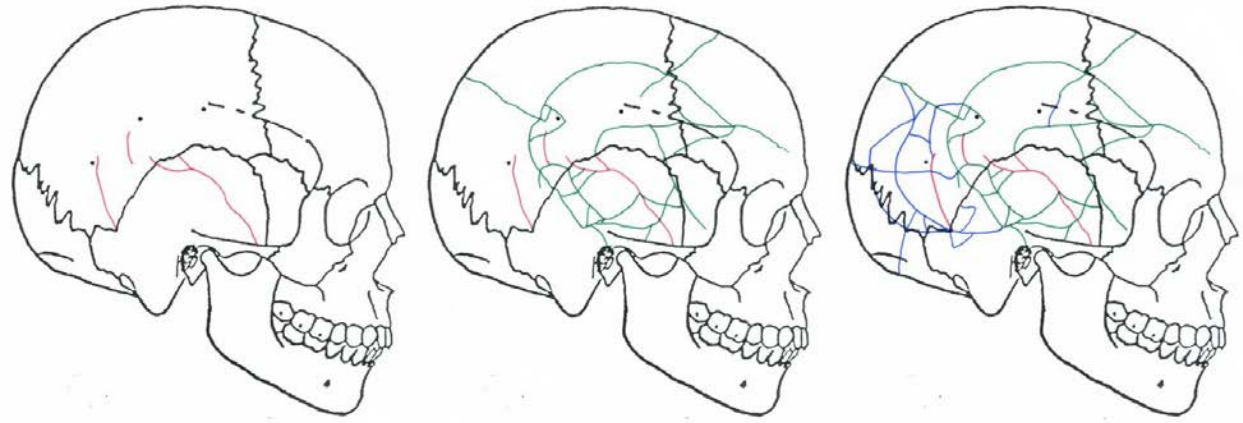

Appendix 4: Comparison of three-dimensional models with resultant fracture patterns.

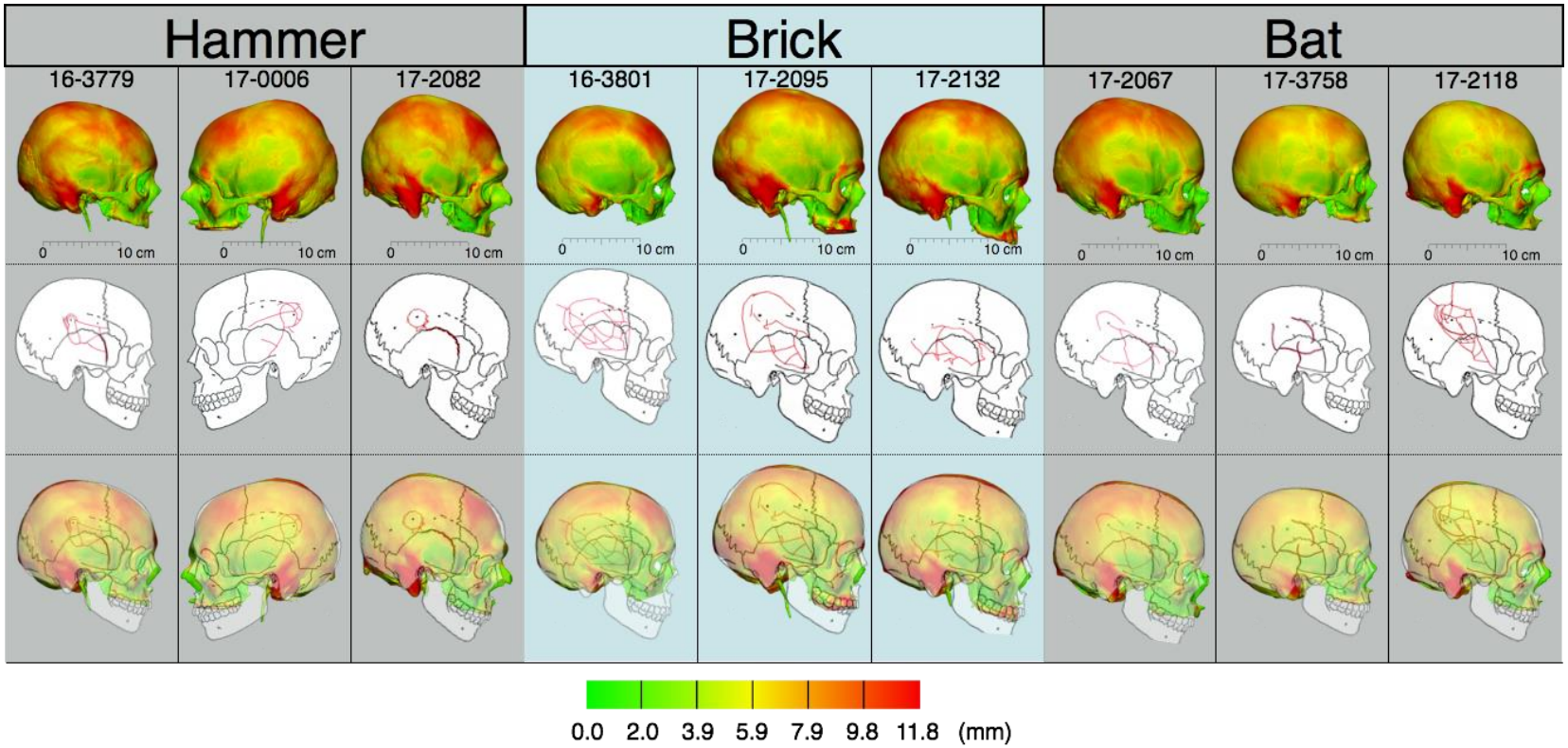

Figure 1. Nine of eighteen thickness distribution maps compared to resulting fracture patterns.

This resource was prepared by the author(s) using Federal funds provided by the U.S. Department of Justice. Opinions or points of view expressed are those of the author(s) and do not necessarily reflect the official position or policies of the U.S. Department of Justice.

Appendix 5: Key outcomes of computational modeling

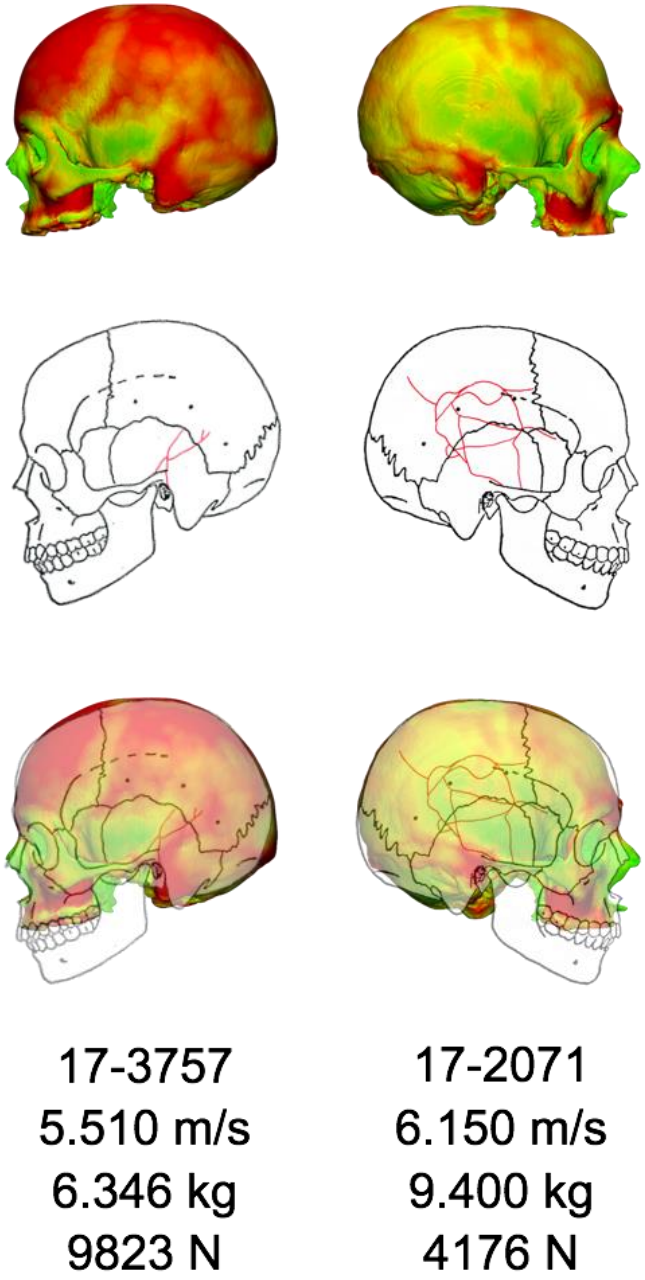

Figure 1. Comparison of fracture patterns between exceptionally thick specimen (left) and exceptionally thin specimen (right). Both received focal (hammer) impacts at different energies. Specimen 17-3757, a specimen with increased thickness, demonstrated linear remote fractures. Specimen 17-2071, a specimen with reduced thickness, demonstrated diffuse fractures. Both of these specimens, each at the extreme ends of the thickness distribution, deviate from the focal, depressed fracture pattern more typical of hammer type impacts.

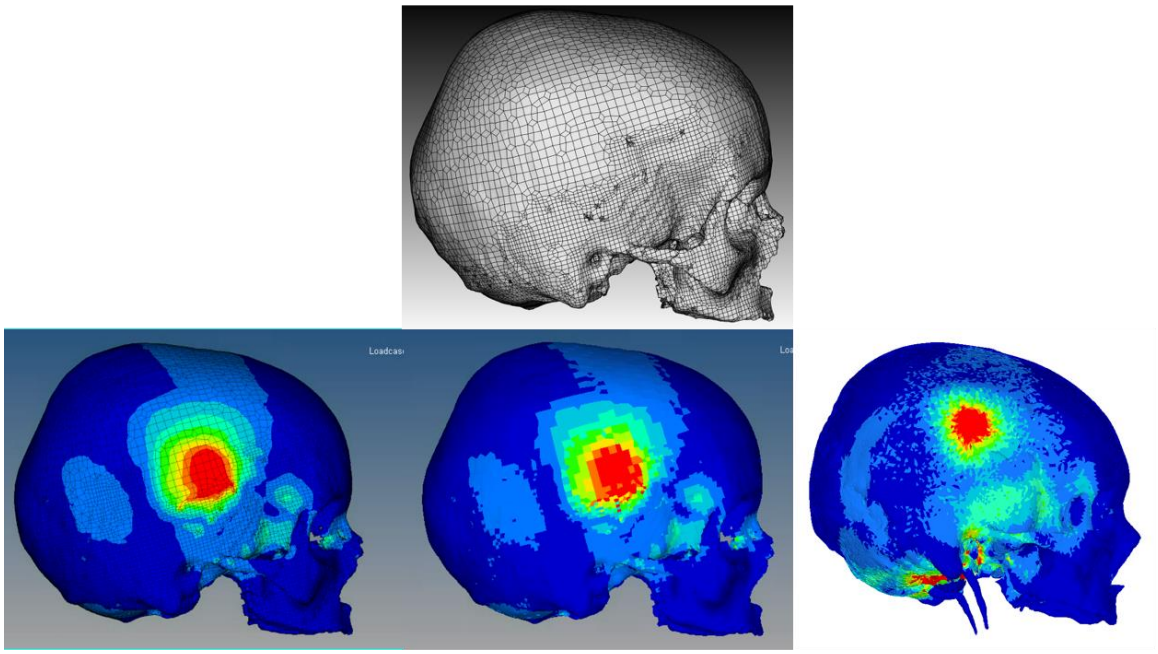

Figure 2. Hexahedral mesh (top row) and simple averaged hexahedral results (bottom left) compared to hexahedral results (bottom middle) compared to tetrahedral results (bottom right) derived from similar inputs.

This resource was prepared by the author(s) using Federal funds provided by the U.S. Department of Justice. Opinions or points of view expressed are those of the author(s) and do not necessarily reflect the official position or policies of the U.S. Department of Justice.

Appendix 6: Impact data for entrapped center-parietal impact experiments.

Specimen	Implement	Mass (kg)	Drop Height (cm)	Peak Force (N)
14-1786	1 in Sphere	10.01	41	5469.2
16-3686	1 in. Sphere	10.01	30	5966.1
14-2111	1 in. Square	10.17	54	5351.1
14-1987	2 in. Hemisphere	10.26	51	7282.8
16-3675	2 in. Hemisphere	10.26	65	5227.6
16-3703	2 in. Hemisphere	10.26	41	5214.0
14-2035	1 in. Square	10.19	74	11826.2
16-3684	1 in. Square	10.17	38	5501.8
16-3698	1 in. Square	10.17	54	7767.4
14-1792	3 in. dia. Flat	10.30	119	8770.6
14-1822	3 in. dia. Flat	10.30	72	8981.7
14-1865	3 in. dia. Flat	10.30	52	8359.9

Appendix 7: Impact data for free-motion center-parietal impact experiments.

Specimen	Implement	Trolley Mass (kg)	Pre-Impact Velocity (m/s)	Post-Impact Velocity (m/s)	Input Energy (J)	Energy Absorbed (J)	Overall Peak Force (N)	Displacement at Peak Force (mm)	Time to Peak Force (s)
18-1109	2 in. Hemisphere	6.31	6.75	3.16	143.8	112.3	9532.6	4.78	0.0007
18-1092	2 in. Hemisphere	6.31	7.23	3.12	165.0	134.3	6361.4	15.33	0.0024
18-1101	2 in. Hemisphere	6.31	6.78	3.98	145.1	95.1	4655.0	15.71	0.0025
18-1083	1 in. Square	6.29	7.58	4.10	180.7	127.8	13641.8	5.54	0.0007
18-1158	1 in. Square	6.29	6.78	2.65	144.6	122.5	14137.3	6.61	0.0010
18-3659	1 in. Square	6.29	7.45	3.35	174.6	139.3	12498.8	8.81	0.0012
18-2219	3 in. dia. Flat	6.53	6.73	2.28	147.8	130.8	8904.0	8.08	0.0013
18-3930	3 in. dia. Flat	6.53	8.14	4.41	216.2	152.7	7087.7	4.43	0.0006
18-2261	3 in. dia. Flat	6.53	8.01	4.56	209.3	141.5	8791.4	6.62	0.0008
18-2361	3 in. dia. Flat	6.53	7.04	3.68	161.7	117.5	8012.1	3.00	0.0004

Appendix 8: Fracture initiation in single impacts to the center parietal.

Interface	Specimen	Initiation and Propagation
1” Sphere (n=2)	16-3686*	The impact produces a shallow depression at the POI.
	14-1786	The impact produces a shallow depression at the POI.
2" Hemisphere (n=3)	16-3703*	The impact produces a shallow depression at the POI.
	16-3675*	A linear fracture initiates at the POI and travels medially to a pre-existing tumorous lesion in the left parietal. Next, a peripheral linear fracture travels from this lesion to the POI as a POI linear fracture propagates to the coronal suture. The impact also produces a circular depression at the impact site and a concentric fracture surrounding the POI.
	14-1987	A peripheral linear fracture initiates at the squamosal suture and travels back to the POI. Next, a concentric fracture forms around the POI.
1" Square Flat (n=4)	16-3698*	A linear fracture initiates at the POI and travels inferiorly to the squamosal suture. The impact also produces a depressed fracture at the POI.
	14-2111	A linear fracture initiates at the POI and travels anteriorly into the frontal. A concentric fracture forms around the POI. Linear fractures initiate at the POI and travel superiorly toward the sagittal suture and inferiorly toward the squamosal suture.
	16-3684*	A peripheral linear fracture initiates near pterion and propagates back to the POI. This fracture branches parallel to the coronal suture, then travels back to the POI. A concentric fracture forms around the POI. Finally, linear fractures initiate at the POI and travel posteriorly and superiorly.
	14-2035	A single peripheral linear fracture initiates in the sphenoid and travels back toward the POI.
3" Dia. Flat (n=3)	14-1865	A single peripheral linear fracture initiates in the sphenoid and travels back toward the POI.
	14-1822	A peripheral linear fracture initiates in the temporal and propagates back to the POI. Another linear fracture initiates at the POI and travels anteriorly. A concentric fracture forms around the impact site.

	14-1792	A peripheral linear fracture initiates in the temporal and propagates back to the POI. Linear fractures form in the temporal, shattering the bone. A concentric fracture forms around the POI as linear fractures radiate outward from the POI in all directions.

Table 1. Entrapped head impact experiments. Specimens marked * were impacted during the current granting period.

Interface	**Specimen**	**Initiation and Propagation**
2" Hemisphere (n=3)	18-1109	The impact produces a circular depressed fracture at the POI.
	18-1092	The impact produces a circular depressed fracture at the POI. A peripheral-linear fracture initiates at pterion and propagates in two directions, back to the POI and into the sphenoid.
	18-1101	A peripheral-linear fracture initiates in the anterior parietal and travels in two directions, back to the POI and into the sphenoid. Concentric fractures branch from this linear fracture, encircling the POI.
1" Square Flat (n=3)	18-3956	The impact produces only a hairline circular fracture around POI.
	18-1158	A single peripheral linear fracture initiates in the sphenoid and travels back toward the POI.
	18-1083	A linear fracture initiates at the POI and travels into the frontal. A concentric fracture forms superiorly around the POI as linear fractures initiate at the squamosal suture and travel superiorly into the frontal and inferiorly into the temporal. A linear fracture travels superiorly from the inferior temporal to the POI.
3” Dia. Flat (n=4)	18-2219	A single peripheral linear fracture initiates in the sphenoid and travels back toward the POI.
	18-2361	A linear fracture initiates in the sphenoid and propagates back to the POI. Next, a linear fracture initiates at the POI and travels into temporal. A third fracture travels posteriorly between these two fractures. The impact also produces a hairline concentric fracture around the POI.
	18-3930	A linear fracture initiates at the POI and travels inferiorly to the temporal bone. Several subsequent linear fractures initiate at the POI and propagate to the coronal suture, the squamosal suture, and the left parietal. Finally, concentric fractures form around the POI.

18-2261	A linear fracture initiates at the POI and travels into the temporal bone. Subsequently, this impact produces a concentric fracture around the POI and several linear fractures (initiating both at the POI and peripherally), resulting in extensive fragmentation.

Table 2. Free-motion impact experiments.

Appendix 9: Diagrams of fractures in center-parietal single impact experiments.

Entrapped Impact Experiments

1” Sphere Implement (n = 2)
14-1786

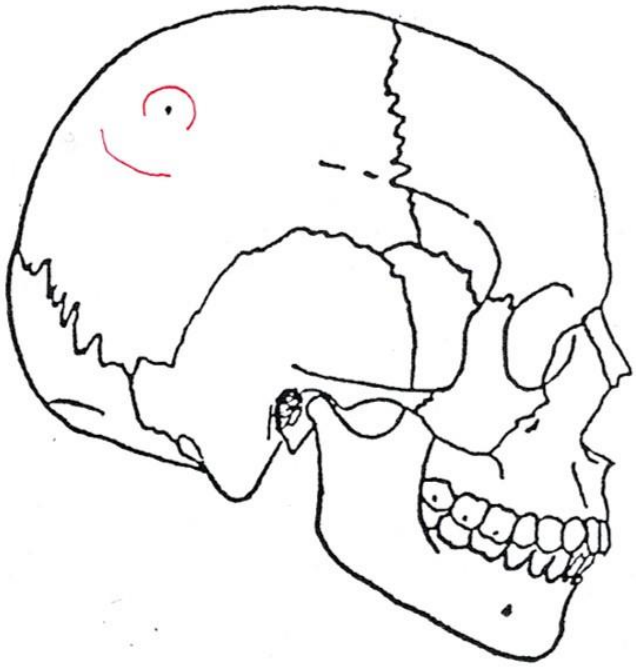

16-3686

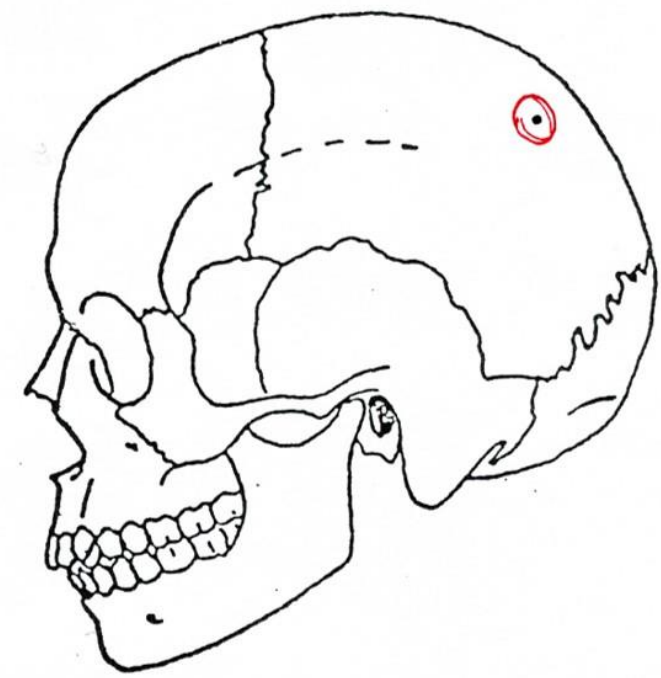

2” Hemisphere Implement (n = 3)
14-1987

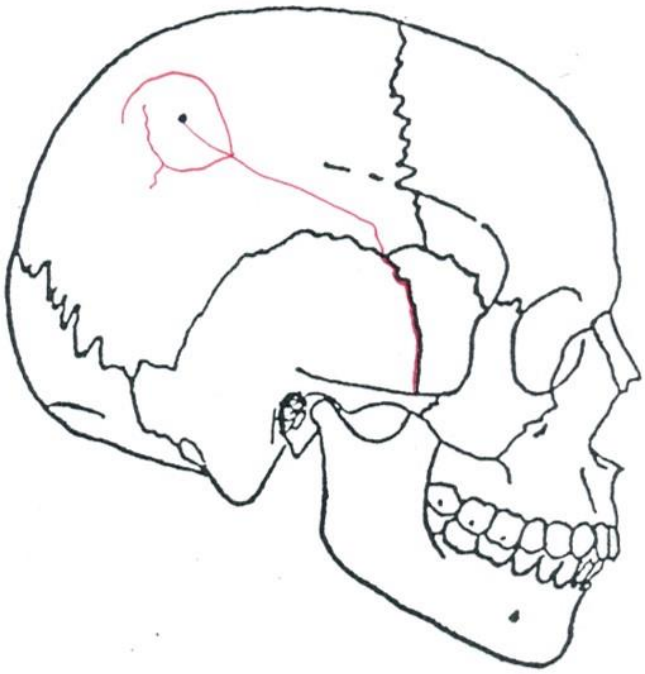

16-3675

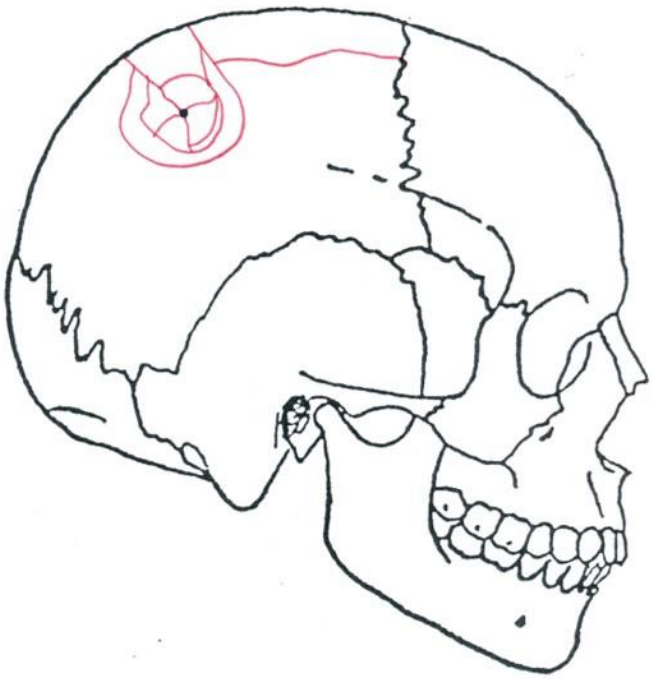

16-3703

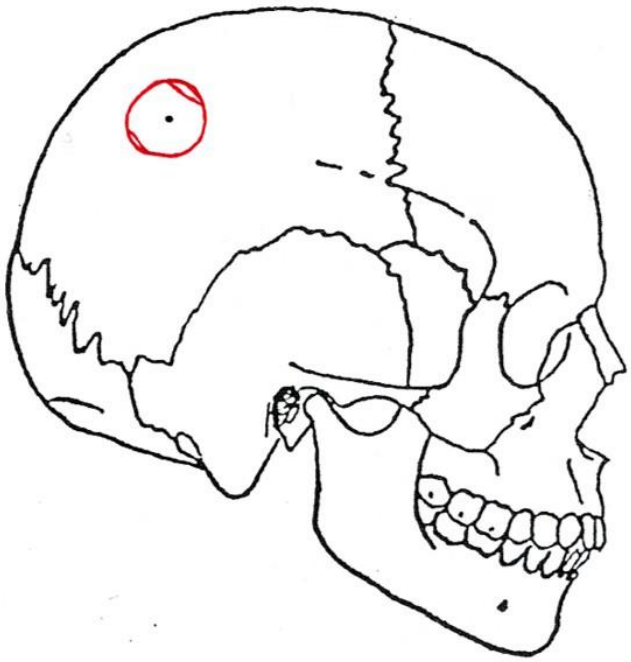

1” Square Flat Implement (n = 4)
14-2035

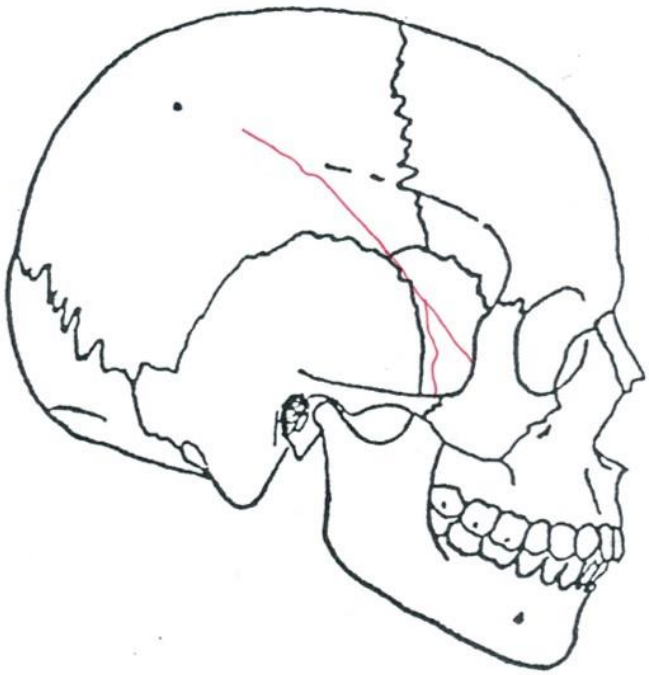

14-2111

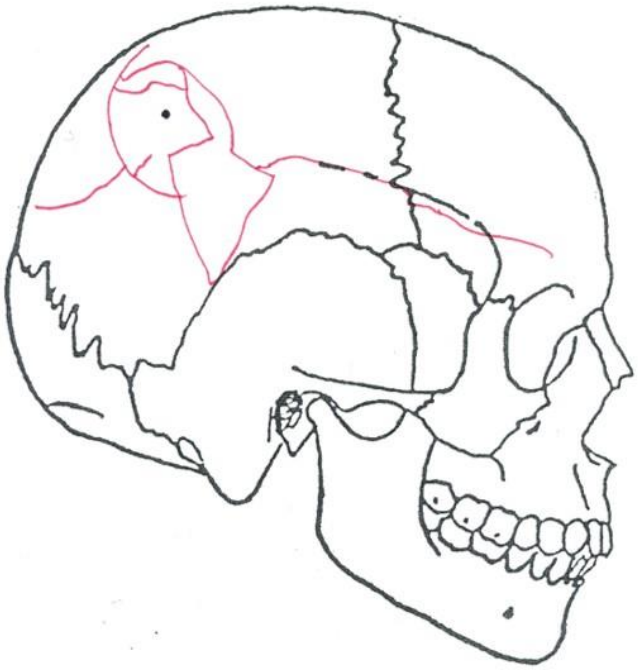

16-3684

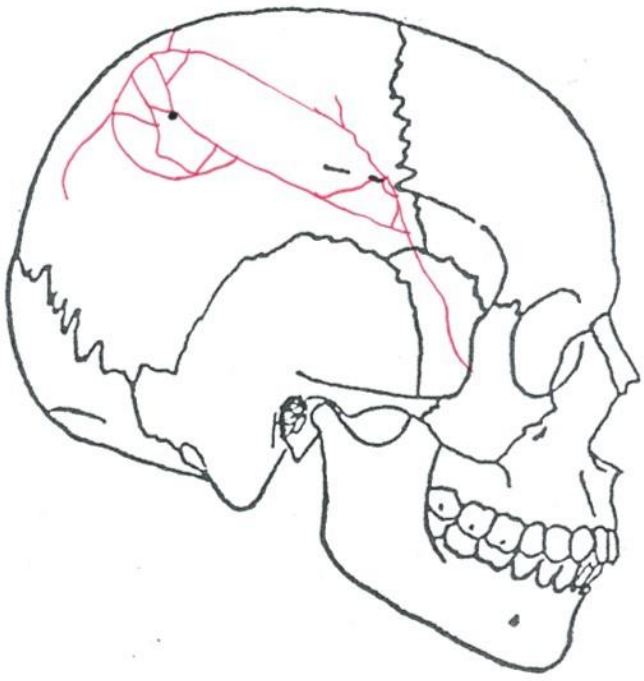

16-3698

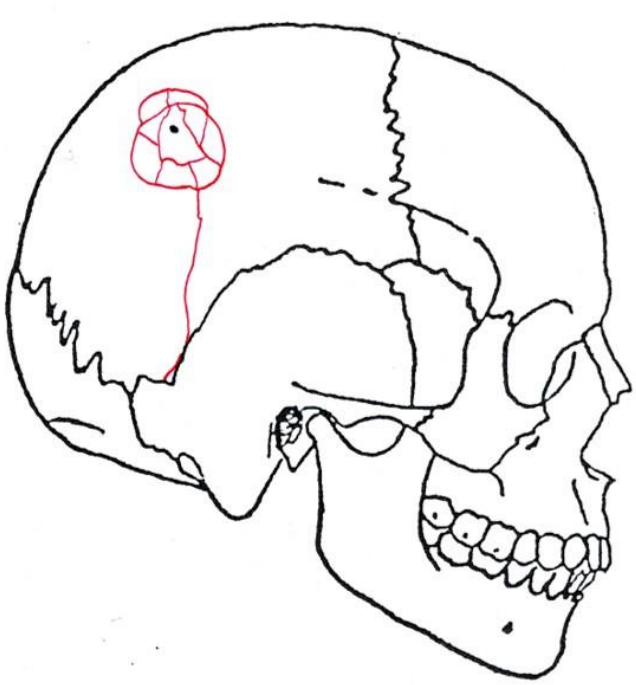

3” Diameter Flat Implement (n = 3)
14-1792

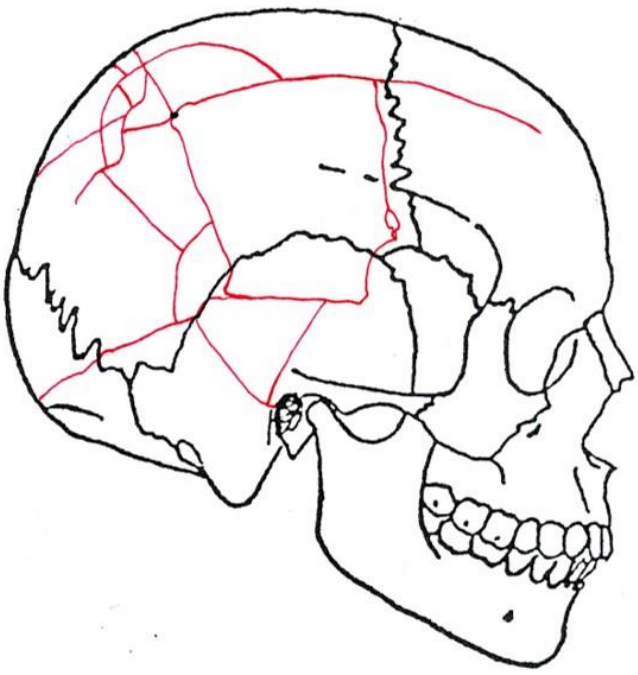

14-1822

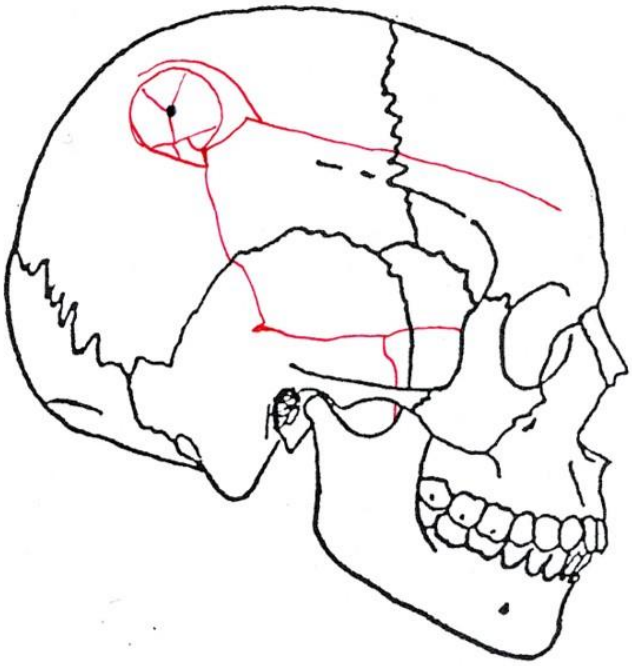

14-1865

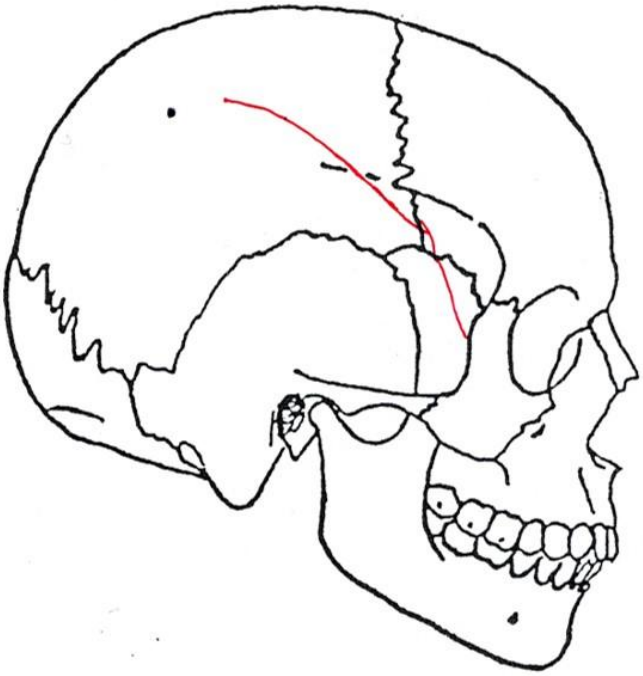

Free-Motion Impact Experiments

2” Hemisphere Implement (n = 3)

18-1092

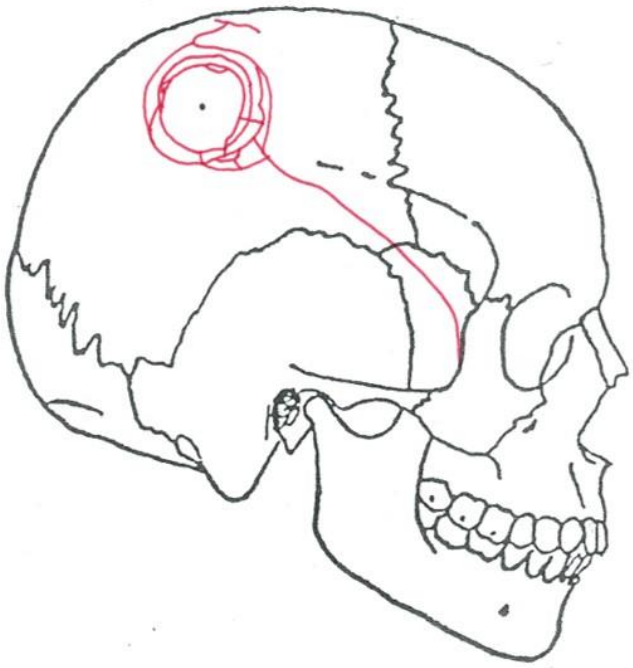

18-1101

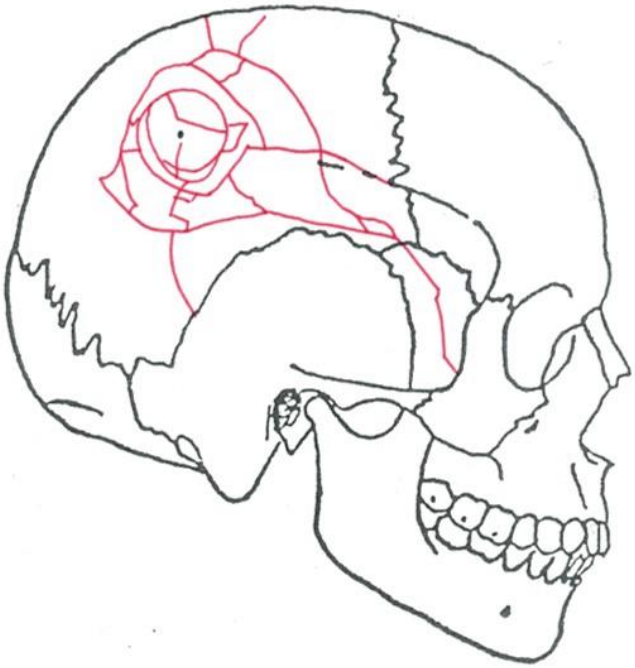

18-1109

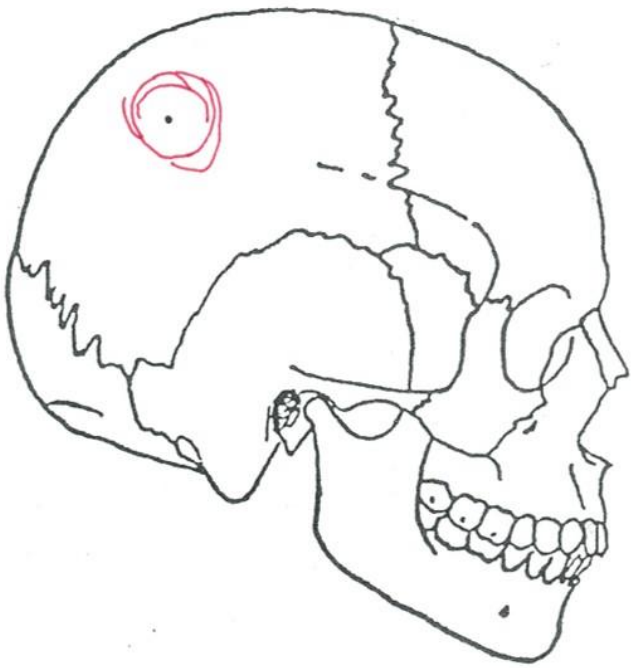

1” Square Flat Implement (n = 3)
18-1083

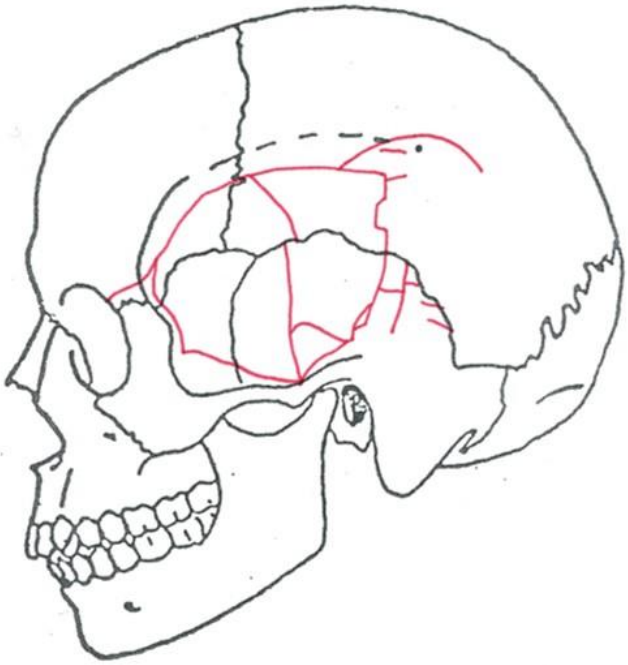

18-1158

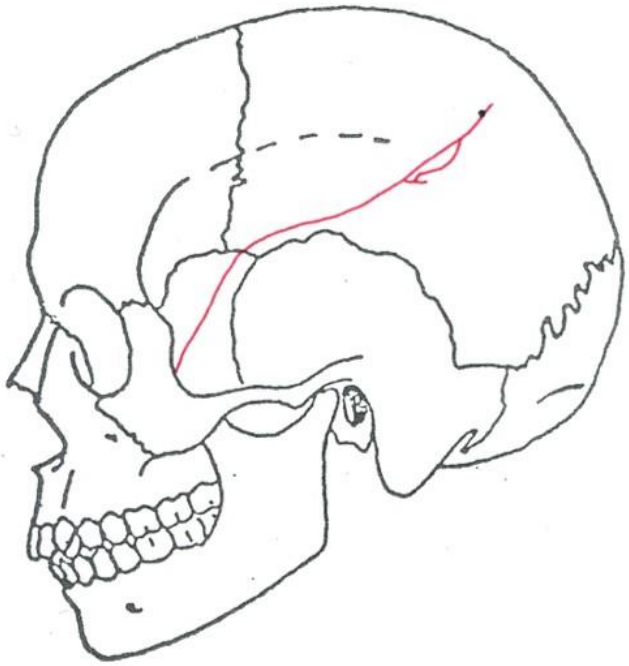

18-3956

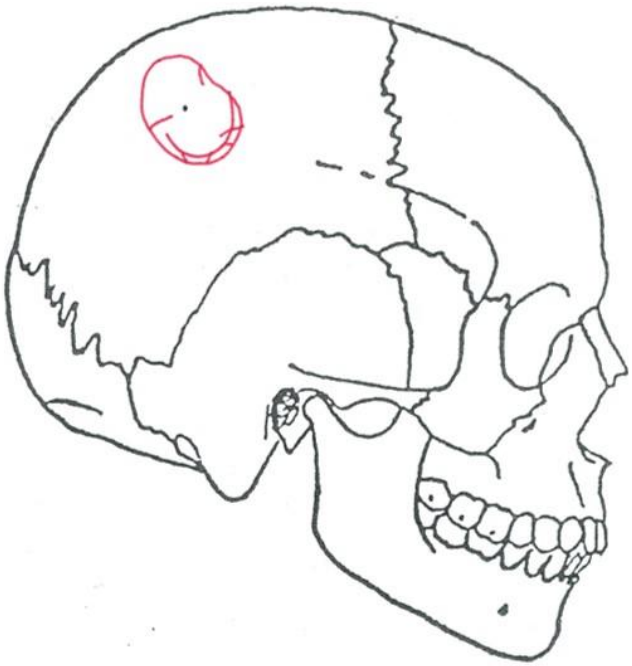

3” Diameter Flat Implement (n = 4)

18-2219

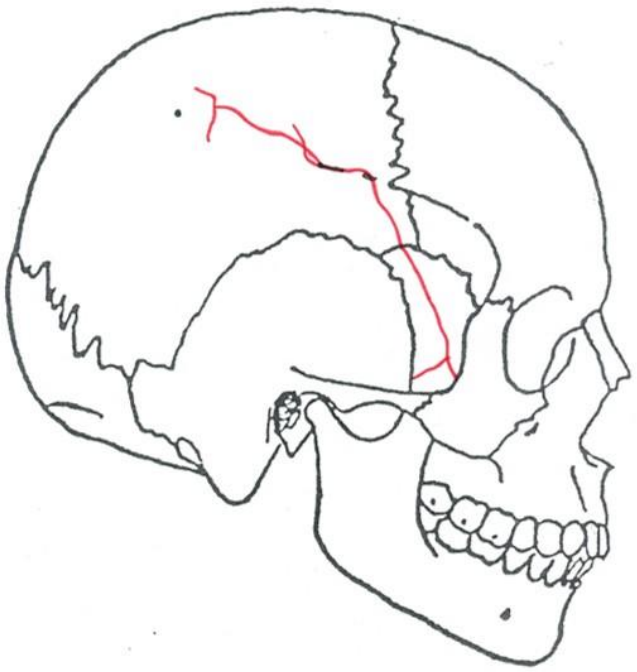

18-2261

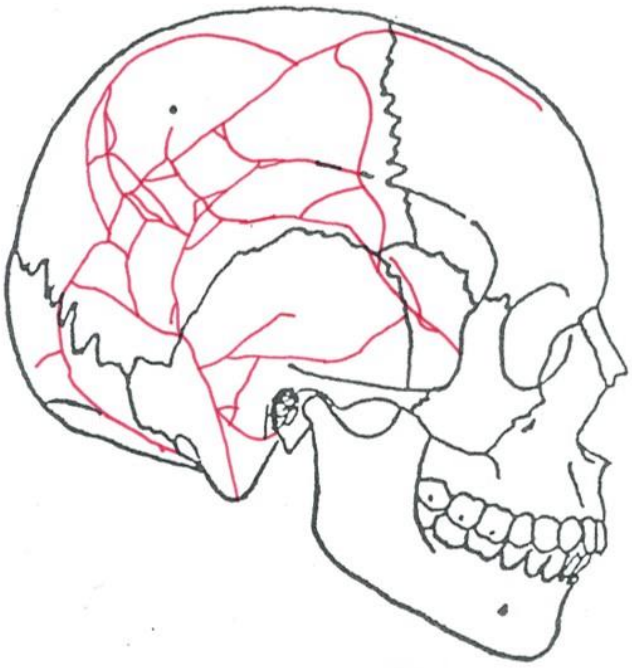

18-2361

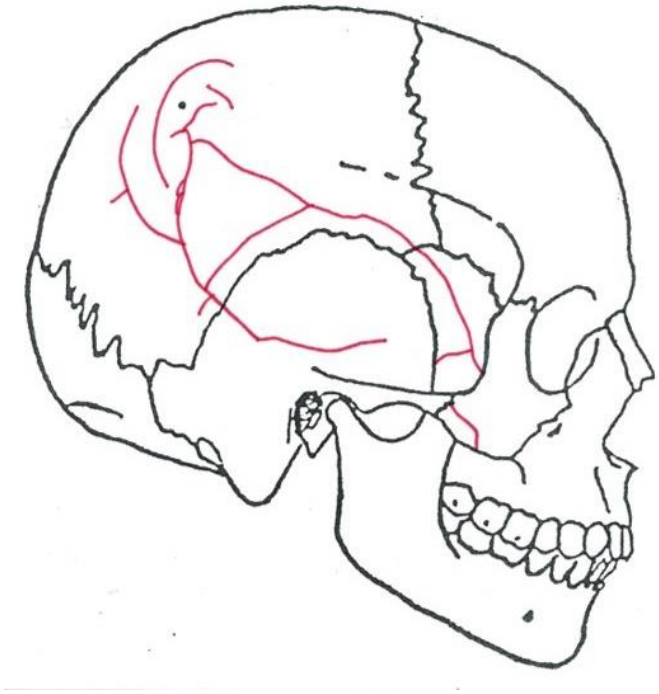

18-3930

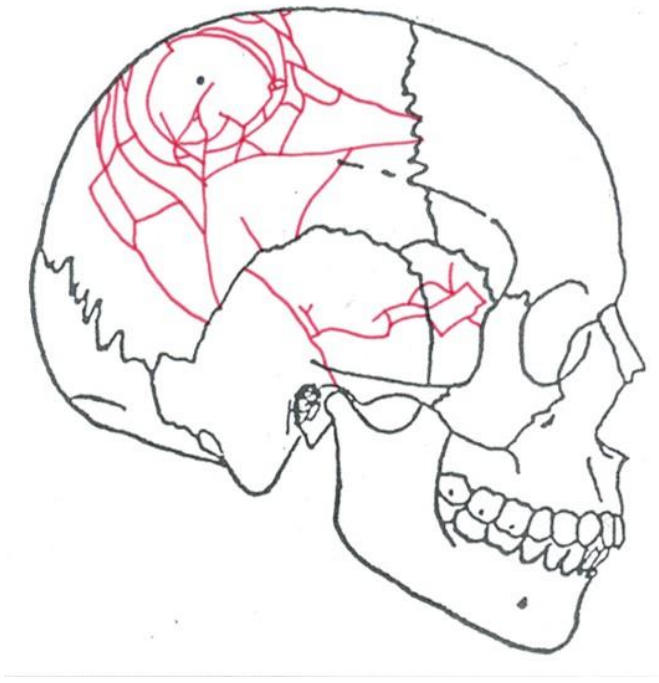

Appendix 10: Mandible impact data.

Specimen	Location	Trolley Mass (kg)	Pre-Impact Velocity (m/s)	Post-Impact Velocity (m/s)	Input Energy (J)	Energy Absorbed (J)	Peak Force (N)
17-2076	Midline	6.435	7.59	6.14	185.4	64.1	4255.6
18-2219	Midline	6.445	7.26	3.59	169.9	128.3	2625.5
18-3930	Midline	6.445	8.65	7.15	241.1	76.4	3874.4
17-0006	L Canine	6.526	5.10	1.28	84.9	79.5	2488.2
17-2095	L Canine	6.435	9.00	6.04	260.6	143.2	5038.9
18-0364	L Canine	6.473	10.08	6.69	328.8	184.0	9669.7
17-2071	LM1	6.435	8.87	4.83	253.1	178.1	3020.4
17-2081	LM1	6.435	7.24	3.34	168.7	132.8	2155.7
18-0361	LM3	6.473	9.39	7.62	285.4	97.4	2519.6
17-2132	LM3	6.435	5.88	3.36	111.2	74.9	1558.4
18-1158	L Ramus	6.445	7.23	3.58	168.4	127.1	3593.4
18-1083	L Ramus	6.445	7.35	4.36	174.1	112.8	4717.4
18-1109	L Ramus	6.445	7.40	5.06	176.5	94.0	3012.4

Appendix 11: Mandible fracture data.

Specimen	Location	AOCMF Code	Fracture #	R Condyle	R Angle	R Body	Symphysis	L Body	L Angle	L Condyle
17-2076	Midline	91-B.S.P	3			x	x			x
18-2219	Midline	91-P.S.P	3	x			x			x
18-3930	Midline	91-P.B.S.B.P	5	x		x	x	x		x
17-0006	L Canine	91-m.B	1					x		
18-0364	L Canine	91-m.B	1					x		
17-2095	L Canine	91-P.m.B	2	x				x		
17-2081	L M1	91-m.A	1						x	
17-2071	L M1	91-m.B	1					x		
18-0361	L M3	91-m.A	1						x	
17-2132	L M3	91-S.A	2				x		x	
18-1158	L Ramus	91-B.m.P	2			x				x
18-1109	L Ramus	91-m.B.P	2					x		x
18-1083	L Ramus	91-B.m.B.P	3			x		x		x

Appendix 12: Dissemination of research findings.

2018 Goots AC, Isa MI, Fenton TW, Watson EO, Vaughan PE, Wei F, and Haut RC. **Estimating Points of Impact in Multiple Blunt Force Cranial Trauma: Lessons From Experimental Impacts.** Presented at the American Academy of Forensic Sciences 70th Annual Scientific Meeting. Seattle, WA. February 19-24, 2018.

After attending this presentation, attendees will gain awareness of: (1) the influence of implement shape on fracture patterning in multiple, blunt cranial impact experiments; and, (2) the implications of this study for fracture pattern interpretation in a medicolegal setting.

This presentation will impact the forensic science community by presenting ground-truth data for multiple cranial impacts with known implements and known number and location of impacts.

The forensic literature is conspicuously lacking in guidelines for locating points of impact and, thus, accurately estimating number of impacts in cases involving blunt cranial trauma. The current study investigates the related issues of estimating locations and number of impacts in a series of multiple blunt force impact experiments on human cadaver heads. Research questions included: (1) Can fracture patterns be used to accurately locate all points of impact?; and, (2) How might implement shape influence practitioners' ability to make this assessment?

Controlled impact experiments were performed on 12 unembalmed, unconstrained human cadaver heads using a pneumatic impact system. Three aluminum impactors were selected to investigate implement effects on fracture patterns: a hammer (1"-diameter flat implement; n=4 specimens), a baseball bat (2.5"-diameter cylinder; n=4), and a brick (3"-diameter flat implement; n=4). Three impacts were delivered to each head: first to the mid-parietal, second to the anterior parietal, and third to the posterior parietal. After each impact, fractures were photographed and diagrammed. Following this series of three impacts, each cranium was macerated and a modified craniotomy cut was made to enable ectocranial and endocranial assessment of fracture.

Input energy for the impact experiments was 105.33J±19.48J for the hammer implement, 112.06J±3.70J for the bat, and 91.81J±18.7J for the brick. Energy differences between implements were non-significant.

The results indicated that sole reliance on ectocranial fractures may lead to an incorrect assessment of location and even a possible overestimation of the number of impacts. In contrast, assessment of only endocranial fracture, in this case internally beveled "bone plugs," may underestimate impact number.

Combined ectocranial and endocranial data provided clear indication of impact location for most impacts with the hammer implement. Nine of 12 impact sites exhibited circular fractures circumscribing the Point Of Impact (POI) ectocranially, 8/12 impact sites exhibited endocranial bone plugs, and 6/12 impact sites exhibited both. One or both features were present in association with known POI at 11/12 impact sites.

The bat produced semicircular fractures partially circumscribing the POI in 5/12 impacts, bone plugs in 3/12 impacts, and both features in 2/12 impacts. One or both features were observed in association with the known POI in 6/12 impacts. In all four specimens, at least one impact site was obscured due to the absence of circular fractures around the POI, presence of linear fractures distant from the POI, and/or lack of bone plugs associated with the POI.

The brick produced semicircular fractures surrounding the POI in 5/12 impacts, bone plugs in 1/12 impacts, and both features in 1/12 impacts. One or both features were observed in association with known POI in 5/12 impacts. In all four specimens, at least one impact site was obscured because: (1) fractures were linear and initiated at sutures adjacent to the POI (2/4 specimens); (2) new fractures intersected with fractures generated in previous impacts (4/4 specimens); and/or, (3) few endocranial defects were observed (4/4 specimens).

The results of this study suggest that practitioners should consider both endocranial and ectocranial data when assessing cranial blunt force trauma. In this experimental set, ectocranial circular defects and endocranial "bone plugs" were consistently observed in association with known points of impact. These features were observed in most hammer impacts, but only about half of the bat and brick impacts. This indicates that implement shape can affect assessment of impact location and, potentially, the number of impacts to an adult human head.

This project was supported by the National Institute of Justice, Office of Justice Programs, United States Department of Justice. The opinions, findings, and conclusions or recommendations expressed in this presentation are those of the authors and do not necessarily reflect the views of the Department of Justice.

2018 Isa MI, Fenton TW, Goots AC, Watson EO, Vaughan PE, Wei F and Haut RC. **Initiation and Propagation of Fractures in Blunt Impacts to Unconstrained Human Cadaver Heads.** Presented at the American Academy of Forensic Sciences 70th Annual Scientific Meeting. Seattle, WA. February 19-24, 2018.

After attending this presentation, attendees will be informed about cranial fracture initiation and propagation in blunt impacts to upright, unconstrained cadaver heads.

This presentation impacts the forensic science community by adding to their current understanding of the relationship between location of fracture production, propagation of fracture, and implement type in cases involving blunt cranial trauma.

Previously, this research group presented the results of blunt cranial impacts performed on entrapped human cadaver heads at the American Academy of Forensic Sciences meetings.1,2 High-speed footage of these experiments support Gurdjian's predictions that: (1) cranial fracture can initiate either at or peripheral to the impact site; and, (2) variables, including implement shape and impact energy, influence the location of fracture initiation and propagation.3 Fenton et al. and Isa et al. report that fractures tend to initiate peripherally in impacts with larger, broader implements and at the point of impact with smaller, more focused implements.1,2 As these experiments were performed on heads fully constrained within a rigid medium (plaster of Paris), it remains unclear how fractures would initiate and propagate in impacts to more realistically constrained heads.

The current study investigated fracture initiation and propagation in blunt cranial impact experiments designed to simulate a blow to the head of an upright individual. Nineteen unembalmed male cadaver heads were impacted using a new, custom-built pneumatic impact system. Three aluminum impactors were selected for this study to approximate the shapes of objects commonly implicated in forensic cases: a brick (3" diameter flat), a bat (2.5" diameter cylinder), and a hammer (1" diameter flat). Twelve impact experiments (n=4 for each implement) were performed at a base energy level: 91.8J±18.7J for brick impacts, 112.1J±3.7J for bat impacts, and 105.3J±19.5J for hammer impacts. Seven impact experiments (n=2 brick;

n=2 bat; n=3 hammer) were performed at approximately 1.6-1.8 times the base energy level (153.6J±50.0J for brick impacts, 137.1J±39.3J for bat impacts, and 172.0J±10.6J for hammer impacts).

Impacts were delivered at the mid-parietal, inferior to the parietal boss, on heads placed in an upright position. Prior to impact, specimens were secured at the C4 vertebra to a mounting plate using an adjustable clamping mechanism. Heads were positioned for impact via breakaway tethers attached to a collar fastened around the neck. A high-speed camera captured fracture initiation and propagation at 10,000fps.

A key result of the base energy-level experiments was the observation of peripheral fracture initiation in impacts with all three implements. These results indicate peripheral initiation is not just possible, but likely following a blunt impact to an unconstrained head. A second key finding was that for all three implements, at least one of four experiments generated fractures that initiated peripherally and did not propagate back to the impact site. As a result, 4/12 experiments (2/4 brick, 1/4 bat, and 1/4 hammer impacts) produced fractures concentrated somewhere other than the impact site (primarily in the temporal and sphenoid).

Initial results also indicate that both implement shape and impact energy influence the location of fracture initiation and propagation in unconstrained heads. At the base energy level, experiments with brick and bat implements tended to generate peripherally initiating linear fractures that propagated back toward and/or away from the impact site. At a higher energy, brick and bat implements produced linear fractures that initiated at the point of impact and propagated away. In contrast, high-energy hammer impacts produced peripherally initiating linear fractures that propagated back toward the impact site.

The present study sought to investigate the issue of fracture initiation and propagation in blunt impacts to unconstrained adult heads. Highspeed photography revealed fractures initiating peripherally with all three implements impacted at the base energy level. In some cases, peripherally initiating fractures also traveled away from the point of impact, resulting in fractures located distant from the point of impact. Practitioners, therefore, should be advised that the location of linear fractures does not necessarily correspond with the location of impact.

This project was supported by the National Institute of Justice, Office of Justice Programs, United States Department of Justice. The opinions, findings, and conclusions or recommendations expressed in this presentation are those of the authors and do not necessarily reflect the views of the Department of Justice.

References:

1. Fenton T.W., Isa M.I., Vaughan P., Haut R.C. Experimental and Computational Validations of the Initiation and Propagation of Cranial Fractures in the Adult Skull. Proceedings of the American Academy of Forensic Sciences, 67th Annual Meeting, Orlando, FL. 2015: 80-81.
2. Isa M.I., Fenton T.W., Vaughan P.E., Haut R.C. Understanding the Role of Contact Area in Adult Cranial Fracture Variation. Proceedings of the American Academy of Forensic Sciences, 68th Annual Meeting, Las Vegas, NV. 2016: 131.
3. Gurdjian E.S., Webster J.E., Lissner H.R. The mechanism of skull fracture. Radiology. 1950:54(3):313-58.

2019 Isa MI, Fenton TW, Goots AC, Wei F, and Haut RC. **Experimental Investigation of Blunt Force Fracture in the Human Mandible.** Submitted for presentation at the American Academy of Forensic Sciences 71st Annual Scientific Meeting. Baltimore, MD. February 18-23, 2019.

After attending this presentation attendees will be informed on the results of experimental blunt impacts to human mandibles. This presentation impacts the forensic science community by providing baseline data associating known points of mandibular impact with resultant fracture patterns.

Available literature on mandible fractures can largely be categorized into 1) clinical studies aimed at evaluating frequencies of fracture types, or 2) impact studies aimed at evaluating fracture tolerances. In clinical studies, the precise loading conditions responsible for fracture patterns are unknown. Conversely, tolerance studies typically provide limited information on fracture patterns. The goals of this study were to conduct impacts to human mandibles at five locations, report on fractures produced in each impact, and describe any patterns that emerged.

The experimental sample comprised 13 intact heads from non-edentulous, unembalmed male cadavers. Heads were placed in an upright position using a previously described procedure (1). A 1-inch long, 2.5-inch diameter cylinder with a mass of 6.45 kg was selected as the implement to simulate a single, clenched fist impact. Mandible impacts were performed at an average velocity of 8.06±1.46 m/s and input energy of 216.1±73.5 J, which produced fractures in all cases. Impacts were delivered to the following locations: midline (n=3), anterior body at the canine (n=3), mid-body at M1 (n=2), posterior body at M3 (n=2), and ramus (n=3). All non-midline impacts were performed on the left side. Following experimentation, each mandible was resected and macerated and fracture numbers and locations were assessed. AOCMF standards (2) were applied in assigning fractures to one of nine regions including the left and right condylar processes, coronoid processes, bodies, and angles, and the symphysis.

Peak forces producing fracture showed considerable variation without a clear relationship between impact location and fracture force. Peak forces ranged from 1558.3 to 9669.7 N (mean=3733.0±2056.0 N).

Thirteen mandibular impacts produced fractures in six anatomical regions defined by the AO Foundation Craniomaxillofacial section. No fractures were observed in the coronoid processes or the right mandibular angle.

One key result was that impact location appeared to influence the number of fractures produced. Mandibular body impacts were the only experiments to produce fractures in exactly one location; this was observed in 5/7 cases. In contrast, all ramus and midline impacts generated multiple fractures: fractures were observed at 2-3 locations in ramus impacts and 2-5 locations in midline impacts.

Another key finding was that impact location influenced fracture location. Impacts to the left mandible always produced at least one fracture on the left mandible. All three ramus impacts produced impact-side condylar process fractures and 1-2 additional fractures in the left and/or right mandibular body. Similarly, body impacts consistently produced fractures at or adjacent to the impact site: anterior body impacts generated fractures in the left body; mid-body impacts generated fractures in the left body and angle; and posterior body impacts generated fractures in the left angle. One anterior body impact also produced a right condylar process fracture and one posterior body impact also generated a symphyseal fracture. Midline impacts also produced

some consistent results: all three impacts generated symphyseal fractures and unilateral or bilateral fractures of the articular portion of the condyle. One impact also produced mandibular body fractures.

All impacts produced at least one fracture approximately at the impact site. However, cases with multiple fractures exhibited considerable variation in the location of additional fractures. Furthermore, few impact locations produced unique results. Fractures of the mandibular body, condylar processes, and symphysis were observed in impacts to various sites. Only one result appeared unique to an impact site: mandibular angle fractures only occurred in body impacts. These results indicate that when multiple mandibular fractures are present it is necessary to look to tension and compression features to reconstruct bending direction.

This presentation communicates consistencies and variations in fracture patterns generated in impact experiments to human mandibles. These results contribute a useful comparative sample of known blunt trauma cases for practitioners evaluating mandibular fractures in forensic cases.

This project was supported by the National Institute of Justice, Office of Justice Programs, United States Department of Justice. The opinions, findings, and conclusions or recommendations expressed in this presentation are those of the authors and do not necessarily reflect the views of the Department of Justice.

References

1. Isa MI, Fenton TW, Goots AC, Watson EO, Vaughan PE, Wei F, Haut RC. Initiation and Propagation of Fractures in Blunt Impacts to Unconstrained Human Cadaver Heads. Proceedings of the 70th Annual Meeting of the American Academy of Forensic Sciences; 2018 Feb 19-24; Seattle, WA. Colorado Springs, CO: American Academy of Forensic Sciences, 2018; 70.
2. Cornelius CP, Audigé L, Kunz C, Rudderman R, Buitrago-Téllez CH, Frodel J, Prein J. 2014. The Comprehensive AOCMF Classification System: Mandible Fractures-Level 2 Tutorial. *Craniomaxillofacial Trauma and Reconstruction* 7(Suppl 1):S015-S030.

2018 Snyder P, Wei F, Haut RC, Fenton TW, Rundell S. **Effects of local thickness distribution on skull fracture due to focal and diffuse parietal impacts.** The 8th World Congress of Biomechanics, Dublin, Ireland, July 8-12, 2018.

INTRODUCTION

Large variations in skull thickness, both globally and locally, have been demonstrated in the adult human population [1]. Similarly, large variations in skull fracture patterns have resulted from equivalent loading conditions [2]. Yet, few studies have quantified local skull thickness distributions and compared them with resulting fracture patterns on a specimen by specimen basis. Therefore, the objective of the current study was to evaluate the effects of skull thickness distribution on fracture patterns during both focal and diffuse impacts. It was hypothesized that fracture lines would present along areas of reduced thickness.

METHODS

Blunt impacts were administered to the center of the parietal bone of twelve unembalmed, adult male human crania. The impact instruments simulated a hammer (flat 1-inch diameter, n=7) or a

brick (flat 3-inch diameter, n=5). Pre-impact CT scans were used to capture the three-dimensional geometry of each skull. Forensic anthropologists hand-diagrammed the fracture pattern after each test. Local thickness distribution maps were generated from the CT data of each specimen and compared to the documented fracture patterns.

RESULTS

Mass of the impact trolley ranged from 6.048 to 9.579 kg and impact velocities ranged from 4.968 to 6.280 m/s. Hammer specimen 16-3779 experienced focal fracture at the point of impact, with fracture lines extending anteriorly through the parietal and temporal bones in areas of reduced thickness. Hammer specimens 17-0006 and 17-2082 exhibited similar presentations (Fig. 1). No hammer fracture patterns extended superiorly towards areas of increased thickness. One hammer specimen (17-3827) experienced fracture at the point of impact without anterior extension. The thickest hammer specimen (17-3757) fractured remotely in an anterior temporal area of reduced thickness. In contrast, brick specimens 16-3801, 17-2095, and 17-2132 experienced diffuse comminuted fractures of the temporal and parietal bones. The outline of the diffuse fractured area tracked along transition regions of relative reduced thickness to relative increased thickness. One brick specimen (17-2035) exhibited linear fractures near the point of impact, along the temporoparietal suture, towards the sphenoid. The thickest brick specimen (16-3817) fractured remotely at the sphenoid in an area of reduced thickness.

DISCUSSION

The hypothesis was confirmed for focal impacts. Specifically, during hammer impacts the fracture lines extended anteriorly through the parietal and temporal bones towards the sphenoid, which represent areas of reduced thickness for all skulls. For diffuse impacts, fracture lines tended to outline regions of reduced thickness. These data provide valuable insight into local thickness distribution as one of the many critical factors to consider when determining the location and nature of impacts based on resulting skull fracture patterns.

ACKNOWLEDGEMENTS

NIJ 2015-DN-BX-K013 and Explico Engineering Company.

REFERENCES

1. Got, et al., (1983). SAE 831619
2. Yoganandan, et al., (2004). Clinical Biomechanics, 19.3 p225-239

2018 Snyder P, Rundell S, Fenton TW, Haut RC, Wei F. **Local thickness of the human skull affects patterns of cranial fracture.** The 42nd Annual Meeting of the American Society of Biomechanics, Rochester, Minnesota, August 8-11, 2018.

INTRODUCTION

Differences in skull thickness of more than 300% have been documented in the adult human population [1]. While the effects of global skull thickness on cranial fracture tolerance have been investigated in the literature, computational models have yet to demonstrate the variability of cranial fracture patterns that are observed experimentally under the same mechanical inputs [2,

3]. Such variability may be explained in part, among several factors, by differences in the local thickness distribution of the skulls. It was hypothesized that variations in fracture patterns arising from the same mechanical input would present in areas of reduced skull thickness on a specimen-by-specimen basis.

METHODS

Blunt impacts were administered to the parietal bone of eighteen unembalmed, adult male human crania. Prior to impact, each specimen underwent a high-resolution computed tomography (CT) scan (GE 750HD; 120 kVp; 125 mAs; 0.625-mm slice thickness; 0.49-mm pixels; 512x512 matrix). Sample preparation involved removal of the scalp on the ipsilateral side of impact, with the exception of an island of scalp at the location of impact. Specimens were secured between the third and sixth cervical vertebrae to a horizontal mounting plate (located on the x-y plane) that allowed translation in the x- and y-directions as well as rotation about the z-axis during impact. A positioning collar with breakaway tethers was affixed around the neck to suspend the head in an upright posture. A custom-built pneumatic striker applied fracture-initiating impacts to the temporoparietal region. Three different aluminum impactor geometries were tested: a flat 1-inch diameter implement ("hammer" n = 7), a flat 3-inch diameter implement ("brick" n = 5), and a cylindrical curved 2.5-inch diameter implement ("bat" n = 6). Mass of the impact trolley ranged from 6.048 to 9.593 kg, and impact velocities ranged from 4.968 to 6.280 m/s.

Slightly increased velocities were used to ensure fracture initiation in the "brick" and "bat" impacts. Forensic anthropologists hand-diagrammed the resulting fracture patterns post-impact. Three-dimensional models of each skull were generated from the CT data using thresholding and segmentation operations in Mimics (Materialise NV; Leuven, Belgium). Wrapping operations were performed to eliminate cavities in the diploë layer, allowing a consistent thickness measurement between the cortical layers. Heat map thickness analyses were then scaled and overlaid onto the corresponding fracture diagrams to evaluate the effects of local skull thickness distribution on fracture pattern presentation arising from three different impacting implements.

RESULTS AND DISCUSSION

Local thickness maps from specimens showing typical fracture patterns of each implement were closely overlaid with their corresponding fracture diagrams (Fig. 1). "Hammer" specimens tended to exhibit a focal fracture pattern consistent with the implement's 1-inch diameter at the point of impact. Typically, secondary fracturing propagated anteriorly into the areas of reduced thickness. The thickest "hammer" specimen (17-3757) did not experience focal fracture at the point of impact but fractured remotely in an area of reduced thickness near the external auditory meatus. One of the thinnest "hammer" specimens (17-2071) experienced a diffuse pattern of fracture in the temporoparietal region of reduced thickness. No 42nd Annual Meeting of the American Society of Biomechanics, Rochester, MN, USA, August 8th – 11th, 2018 "hammer" specimens fractured superiorly towards areas of increased thickness. "Brick" specimens tended to exhibit diffuse fracture patterns in the temporoparietal region. The outline of the diffuse area of fracture tracked along transition regions of reduced thickness to regions of increased thickness. One specimen (17-2035) experienced linear type fractures near the point of impact anteriorly towards regions of reduced thickness in the sphenoid. The thickest specimen (16-3817) fractured remotely in the sphenoid region in an area of reduced thickness. "Bat" specimens

tended to exhibit the widest variety and span of diffuse and linear fractures. “Bat” impacts were the only to travel anteriorly into the frontal bone (16-3803, 17-2067, 17-2081), as well as the only to experience significant superior propagation towards the sagittal suture (17-2118). While “bat” specimens 16-3803 and 17-2081experienced more focal fracture near the point of impact with anterior linear fracture propagation, specimens 17-2067, 17-3758, and 17-2118 experienced more diffuse fracture in the area of impact, and 17-4813 experienced more remote linear fracture. In general, “bat” fracture occurred in relative regions of reduced thickness.

CONCLUSIONS

Fractures tend to occur in, and propagate through, regions of reduced thickness. While “hammer” impacts are likely to exhibit focal fracture near the point of impact, “brick” and “bat” impacts are likely to exhibit more diffuse fracture patterns that track along locally thin areas of the skull. In general, the results of the current study have confirmed the hypothesis. Intrinsic skull properties, specifically thickness distribution, play an important role in the patterns of cranial fracture. These findings are important when determining the cause of a skull fracture in a forensic setting.

ACKNOWLEDGEMENTS

NIJ 2015-DN-BX-K013, Explico Engineering Company, and Mr. Clifford Beckett.

REFERENCES

1. Got, C., et al. SAE Technical Paper, No. 831619, 1983.
2. Ruan and Prasad. Stapp Car Crash J, 45.11 p395-414, 2001.
3. Yoganandan, et al. Clinical Biomechanics, 19.3 p225-239, 2004.

2018 Watson EO, Fenton TW, Isa MI, Goots AC, Vaughan PE, Wei F, and Haut RC. **The Influence of Implement Shape on Fracture Pattern and Defect Size in Experimental Blunt Cranial Impacts.** Presented at the American Academy of Forensic Sciences 70th Annual Scientific Meeting. Seattle, WA. February 19-24, 2018.

After attending this presentation, attendees will better understand relationships between Point Of Impact (POI) -involved implement and fracture patterns from single, blunt cranial impacts to unconstrained human cadaver heads.

This presentation will impact the forensic science community by contributing to ground-truth data in support of assessing implement shape and POI in cases involving blunt cranial trauma.

Previous research has demonstrated that implement shape influences location and pattern of fractures in controlled impacts to fully constrained adult human heads and developing porcine specimens.1-3 This current study further investigated the effects of implement shape on fracture patterns in experimental impacts to upright, unconstrained human heads. This study explored two major questions relevant to analyses of blunt cranial trauma: (1) Do different-shaped implements produce distinct fracture patterns?; and, (2) Can fracture patterns be used to estimate the POI? For 12 experimental cases in which implement and POI were known, these questions were explored through analyses of fracture patterns, defect size, and spatial relationship between fractures and the known POI.

Twelve adult male cadaver heads were impacted with a pneumatic impact system that allowed for controlled energy impacts to unconstrained specimens. Single impacts were administered to the mid-parietal, inferior to the parietal boss, with three implements that approximated a hammer (1"-diameter cylinder with a rounded surface; n=4), a baseball bat (2.5"-diameter cylinder with a curved surface; n=4), and a brick or broad, flat implement (3"-diameter flat disk; n=4).

Following single impacts, ectocranial fracture patterns were diagrammed and photographed. To observe endocranial outcomes, adjusted craniotomy cuts were conducted on the crania after maceration. Relevant data collected were: type of fractures present, spatial relationship between fractures and known POIs, and approximate size of any circular-type defects.

Energy to fracture and overall peak force were not statistically different between implements. For all three implements, the average fracture energy was 12.44J±6.04J, and the average overall peak force was 5221N±1936N.

The results of fracture patterns and their relationship with POI revealed trends by implement. In 3/4 impacts with the hammer implement, focal and circular depressed fractures circumscribed the POI. Endocranially, these impacts also generated corresponding internally beveled, delaminated “bone plugs” concentrated under the POI. Such endocranial defects were largely absent in the bat and brick impact experiments. In 3/4 impact experiments with the bat, curvilinear fractures occurred around the POI; however, they did not completely encompass the POI and exhibited an oval shape. The brick implement produced more variable fracture patterns. Half (2/4) of these impacts resulted only in linear fractures located remote from the POI in adjacent bones. In the other two brick impacts, large concentric fractures formed around the POI.

Circular-type defects were produced in 3/4 hammer, 3/4 bat, and 2/4 brick impact experiments. The hammer implement produced defects with the smallest average diameter (29mm±1.15mm.) These defects were of a consistent size, slightly larger than the implement diameter. The brick implement produced the largest defects (59mm±7.07mm); defects were typically smaller than the diameter of the implement. The bat produced defects of an intermediate size (34mm±15.72mm); however, defect sizes were inconsistent and overlapped in range with defects produced by the other two implements. These results indicate that defect size may assist in making a general distinction between small and large implements (i.e., hammer vs. brick), but it may not be possible to infer implement size based on defect size alone.

The results of this study reveal emerging trends in cranial fracture patterns associated with implement shape and suggest some baseline parameters for locating POI. In this experimental sample, an approximately circular defect, particularly in association with an endocranial bone plug, served as an effective indicator of POI. In contrast, when fracture patterns consisted only of linear fractures without the presence of round defects (1/4 hammer, 1/4 bat, 2/4 brick), impact location was obscured.

This project was supported by the National Institute of Justice, Office of Justice Programs, United States Department of Justice. The opinions, findings, and conclusions or recommendations expressed in this presentation are those of the authors and do not necessarily reflect the views of the Department of Justice.

References:

1. Fenton T.W., Isa M.I., Vaughan P.E., Haut R.C. Experimental and Computational Validations of the Initiation and Propagation of Cranial Fractures in the Adult Skull. Proceedings of the

American Academy of Forensic Sciences, 67th Annual Scientific Meeting, Orlando, FL. 2015: 80–81.
2. Isa M.I., Fenton T.W., Vaughan P.E., Haut R.C. Understanding the Role of Contact Area in Adult Cranial Fracture Variation. Proceedings of the American Academy of Forensic Sciences 68th Annual Scientific Meeting, Las Vegas, NV. 2016: 131.
3. Vaughan P.E., Vogelsberg C.C.M., Vollner J.M., Fenton T.W., Haut R.C. 2016. The Role of Interface Shape on the Impact Characteristics and Cranial Fracture Patterns Using the Immature Porcine Head Model. Journal of Forensic Sciences. 61(5): 1190 – 97.